AIMS Geosciences

AIMS Geosciences, 11(3): 651–685.
DOI: 10.3934/geosci.2025028
Received: 10 April 2025
Revised: 30 May 2025
Accepted: 25 June 2025
Published: 01 August 2025

https://www.aimspress.com/journal/geosciences

Research article

DMT-simulation to calibrate a structured-clay model at the Onsøy Geo-Test site, Norway

Lluis Monforte[1], Laurin Hauser[1], Paola Monaco[2], Anna Chiaradonna[2], Sara Amoroso[3], Marcos Arroyo[1,4,*], and Diego Marchetti[5]

[1] Centre Internacional de Mètodes Numèrics en Enginyeria, CIMNE, Barcelona, Spain
[2] Department of Civil, Construction-Architectural and Environmental Engineering, University of L'Aquila, L'Aquila, Italy
[3] University of Chieti-Pescara, Pescara; Istituto Nazionale di Geofisica e Vulcanologia, L'Aquila, Italy
[4] Universitat Politècnica de Catalunya, UPC-BarcelonaTech, Barcelona, Spain
[5] Studio Prof. Marchetti, Rome, Italy

* **Correspondence:** Email: marcos.arroyo@upc.edu; Tel: (+34) 934017254.

Abstract: The Onsøy clay deposit is representative of soft structured natural clays. These are materials with brittle mechanical responses that are important to represent correctly in design. For this purpose, numerical models are employed, but calibration of the appropriate constitutive models is difficult. Calibration based on laboratory tests alone is problematic because the natural structure is damaged during sampling to an extent that is difficult to identify. In this work, we explored a calibration strategy for structured clay models based on the joint interpretation of laboratory and field tests through simulation. For this purpose, we made use of a large strain simulation of two mechanical in-situ test results where probes were pushed into the ground: The cone penetration test (CPTu) and the Marchetti dilatometer (DMT). The results obtained for the Onsøy clay showed that the DMT is advantageous in this respect, because it has lower measurement uncertainty and because the initial membrane contact pressure measured in the test is less sensitive to confounding factors.

Keywords: soft clay; dilatometer; site characterization; numerical modelling; structured soil

1. Introduction

Important deposits of marine soft clays are present worldwide [1,2]. These clays usually have some natural structure that significantly increases their stiffness and strength. Clay structure is thus important for geotechnical engineering applications. Unfortunately, structure is also fragile and difficult to measure during site investigation. This poses a problem for geotechnical site characterization, a problem that is more acute as geotechnical analysis and design is ever more reliant on numerical simulation.

Quite often, a designer may have at hand robust numerical codes, featuring numerous constitutive models, including some that capture the relevant material behavior for the problem. In particular, this is the case for problems involving naturally structured clays. Since [3] proposed a framework to develop elasto-plastic models for structured soils, many such models have been developed, with varying degrees of complexity, successfully incorporating features such as anisotropic behavior [4] or cyclic loading capabilities [5]. However, that same hypothetical designer will also often face severe problems in obtaining reliable key input values to feed into the model (e.g., the amount of structure that is present in the ground). Given calibration difficulties and commercial pressures, designers often had to settle for sub-optimal solutions.

One possible strategy to improve current practice is to extract more model-oriented information from the usual tools of site investigation and, in particular, from in situ tests, like the Marchetti dilatometer (DMT), the cone penetration test (CPTu), or the pressuremeter (PMT). However, this strategy is not without problems. It is true that in situ tests are generally faster and simpler to execute than hydro-mechanical geotechnical laboratory tests, largely because laboratory tests require a sufficient number of samples that are correctly representative of the materials present at the site, and such samples are difficult to obtain. However, the main drawback of in situ tests is that they involve complex and only partly controlled hydro-mechanical loading of the soil, and measured test outcomes are thus difficult to relate unequivocally to particular parameters or properties. As a consequence, the classical interpretation of in situ test results has been highly reliant on empirical correlations. Establishing links between those empirically interpreted results and the inputs required in a realistic constitutive model is possible (e.g., [6]) but generally challenging.

One interesting alternative is offered by using also simulation in the interpretation of the in-situ test. If the same constitutive model that will be employed in geotechnical analyses is consistently applied to analyze the in-situ tests, it is likely that relevant information would be simpler to extract. Until recently, this approach was limited to those in situ tests loading the soil with the smallest amount of disturbance, like geophysical seismic tests, where systematic inversion to extract small-strain properties is routine. For tests that load the soil in the plastic range, only the self-boring pressuremeter was deemed simple enough to analyze numerically (e.g. [7,8]). However, self-boring pressuremeter tests are relatively rare tests, with results highly dependent on operator skill.

This situation has changed with improvements in numerical technology. Realistic geometric simulation of CPTu tests using advanced constitutive models has now become possible (e.g., [9,10]). Other tests, like the DMT, are more challenging, but recently, some reasonable approximations have been proposed for the insertion phase [11]. Effective simulation of those more popular tests has opened the way to address more complex model calibration problems (e.g., [12]).

In this work, we demonstrate this idea, calibrating a model appropriate for structured natural clays to the Onsøy clay deposit. To achieve this purpose, we combine information from laboratory test results using systematic simulation of CPTu and DMT insertion.

2. Materials and methods

2.1. Description of the dataset

2.1.1. Site overview

The (new) Onsøy geotechnical research site is one of the Norwegian GeoTest Sites (NGTS) established by the Norwegian Geotechnical Institute (NGI) in 2016 [13]. An extensive site investigation campaign has been conducted [13–15], including, among other field tests, numerous cone penetration tests (CPTu) and Marchetti flat dilatometer tests in addition to abundant triaxial tests and oedometer tests from samples recovered from block and tube samplers. This data is openly available online [16]. Data from recent DMT tests are reported by [17]. For this work, we focus on the South East Corner of the site (SEC) where a large cluster of CPTu and DMT data were available, using laboratory results from the closer boreholes in the South Center (SC) area (Figure 1, Figure 2).

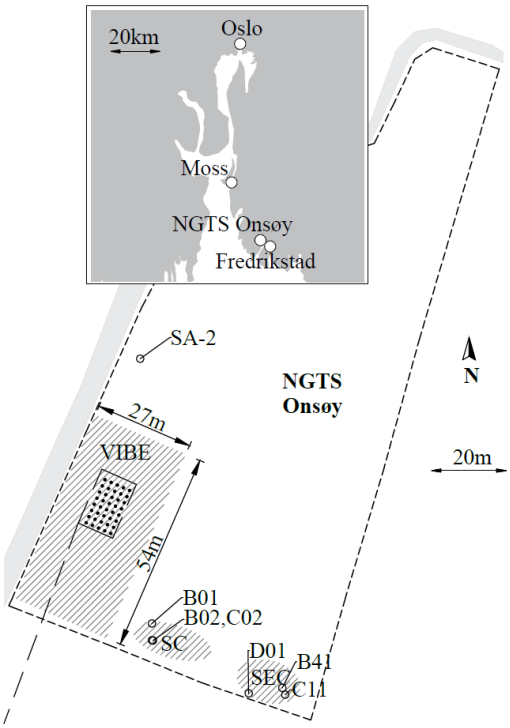

Figure 1. Location and general plan of the Onsøy site [18].

Up to four different clayey units have been identified at the site [13]. The joint and individual thicknesses of these four clayey units are highly variable across the site. The depth to bedrock is 8 m at the southwest corner (SWC) [18], 22 m in the South Center (SC), and 28 m in the south east corner

(SEC) [13]. The first unit (Unit I) has a thickness of approximately 1 m and corresponds to a weathered clayey crust. Unit II is composed of a clay (65% clay/35% silt) with a plasticity index around 44% and water content of around 70%. Unit III is siltier (approximately 50% clay/50% silt), has lower plasticity (plasticity index around 27%), and is less porous, with water content of around 45%. The fourth unit (Unit IV) has similar index properties to Unit II.

However, apart from the first meters of weathered clay crust, the different clay units are not apparent in either the cone (see below) or the DMT records [17,19,20] (see also results below). This somewhat surprising fact is taken here as a starting point, and, in what follows, we make no distinction between clay units.

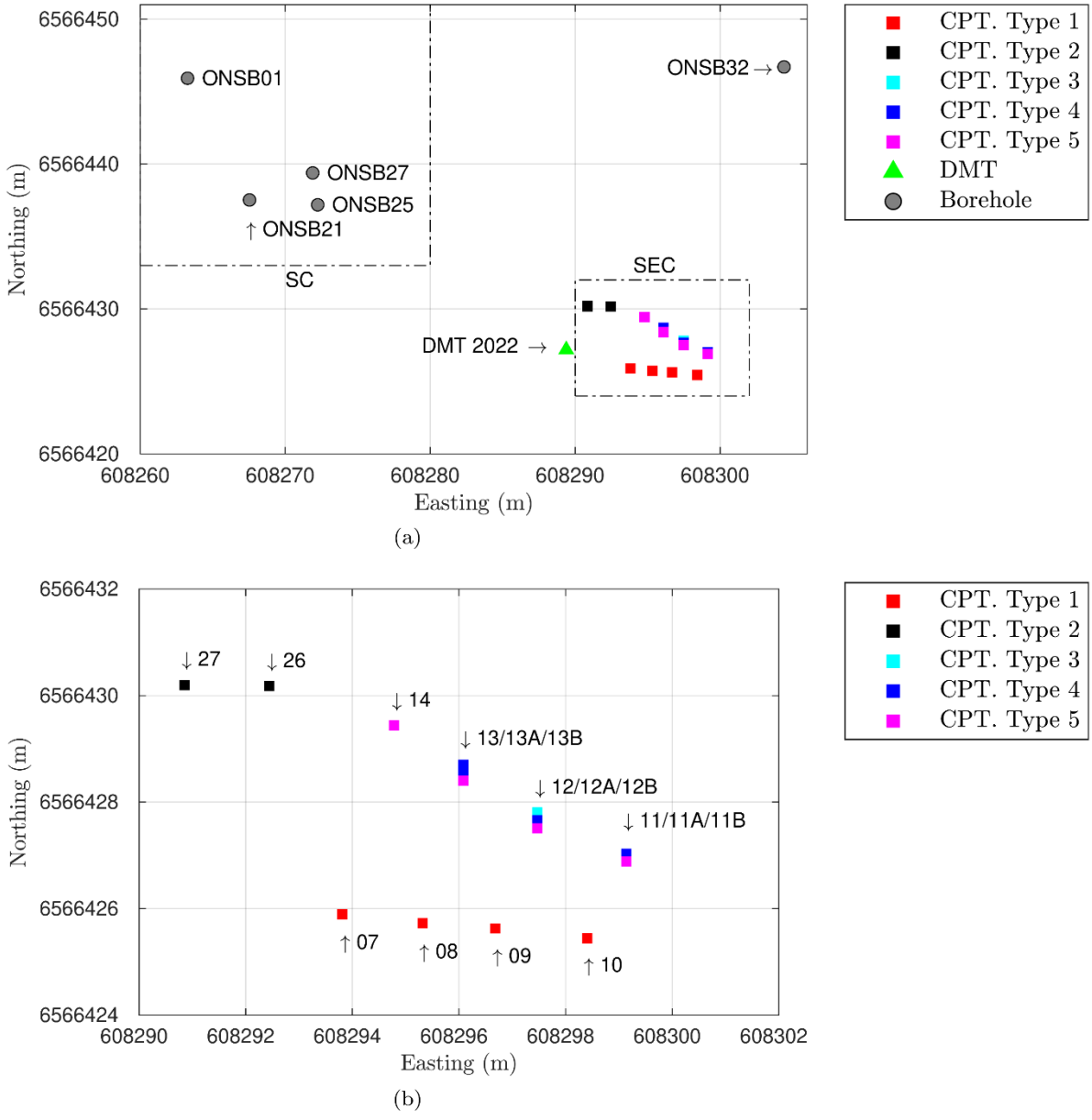

Figure 2. Onsøy site. (a) Location of the CPTu, DMT, and boreholes considered. (b) Detail of the CPTu test area.

2.1.2. Evidence for structure

Most naturally deposited clays are endowed with a fragile structure that is highly susceptible to sampling damage. This is also the case for Onsøy and is illustrated here by reference to laboratory test results.

Figure 3 presents the results of K_0 consolidated undrained triaxial compression tests for all samples considered, including effective and normalized stress paths and the evolution of deviatoric stress and mobilized friction in terms of axial strain. Results are labeled using conventional sample quality, as assigned in the reports according to the classification of [21]. As it is well established for natural clays [22], the peak undrained strength ratio decreases as sample disturbance increases. Differences in strength are also present at the end of the tests, although now the sense is inverted, with high-quality samples showing lower strength. It should be noted, however, that critical state conditions were not attained in the tests and that there is little information on the precise failure mode of the laboratory specimens (e.g., did they localize in shear or not?). On the other hand, initial stiffness, as measured, for instance, by the strain at which peak conditions are achieved, seems less affected by sample disturbance.

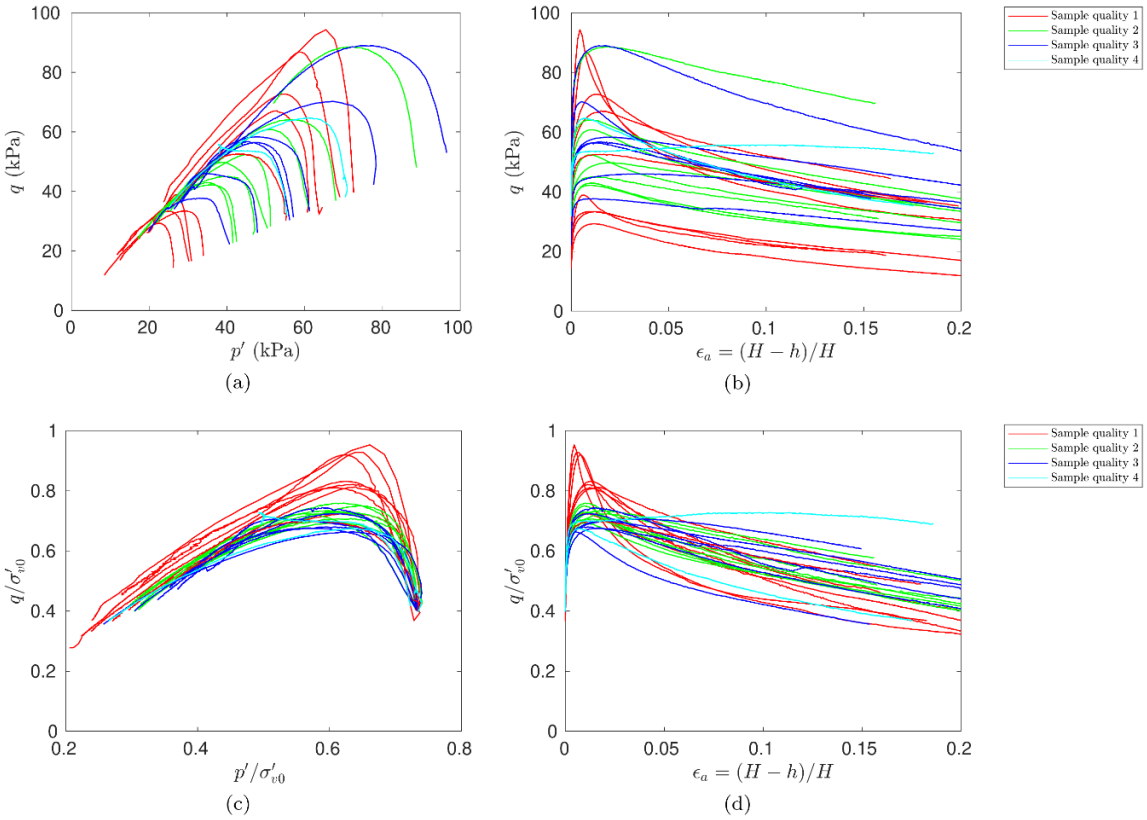

Figure 3. Onsøy site. Undrained triaxial tests on samples of all qualities. Sample quality classification as per [21].

Figure 4 presents the same triaxial results but now only for samples classified in the highest quality category (category 1, as per [21]). Even when considering only high-quality samples, the peak undrained shear strength presents high variability. These category 1 samples include some recovered

using a 250 mm Sherbrooke sampler (borehole ONSB01) and some recovered using a 76 mm piston sampler (SWORD) in ONSB21 or ONSB25. Despite their common classification, the responses are different, with Sherbrooke ONSB01 showing a higher peak strength ratio attained at smaller strains and a more abrupt post-peak fall. Sherbrooke samples are known to cause less disturbance than even the highest quality borehole samplers, as the samples have very large diameter to wall ratios [19].

Sample disturbance obscures any possible trend with depth on peak undrained strength. Normalized peak strength ratios range from $S_u^{peak}/\sigma'_{v0} = 0.35$ to 0.47 (Figure 5). Although there is a hint that Unit II might be somewhat weaker, there are not enough Sherbrooke or high-quality samples to confirm this. The presence of structure and the varied damage levels imposed by different sampling procedures are also clear when the apparent yield stresses from oedometric tests are examined (Figure 6).

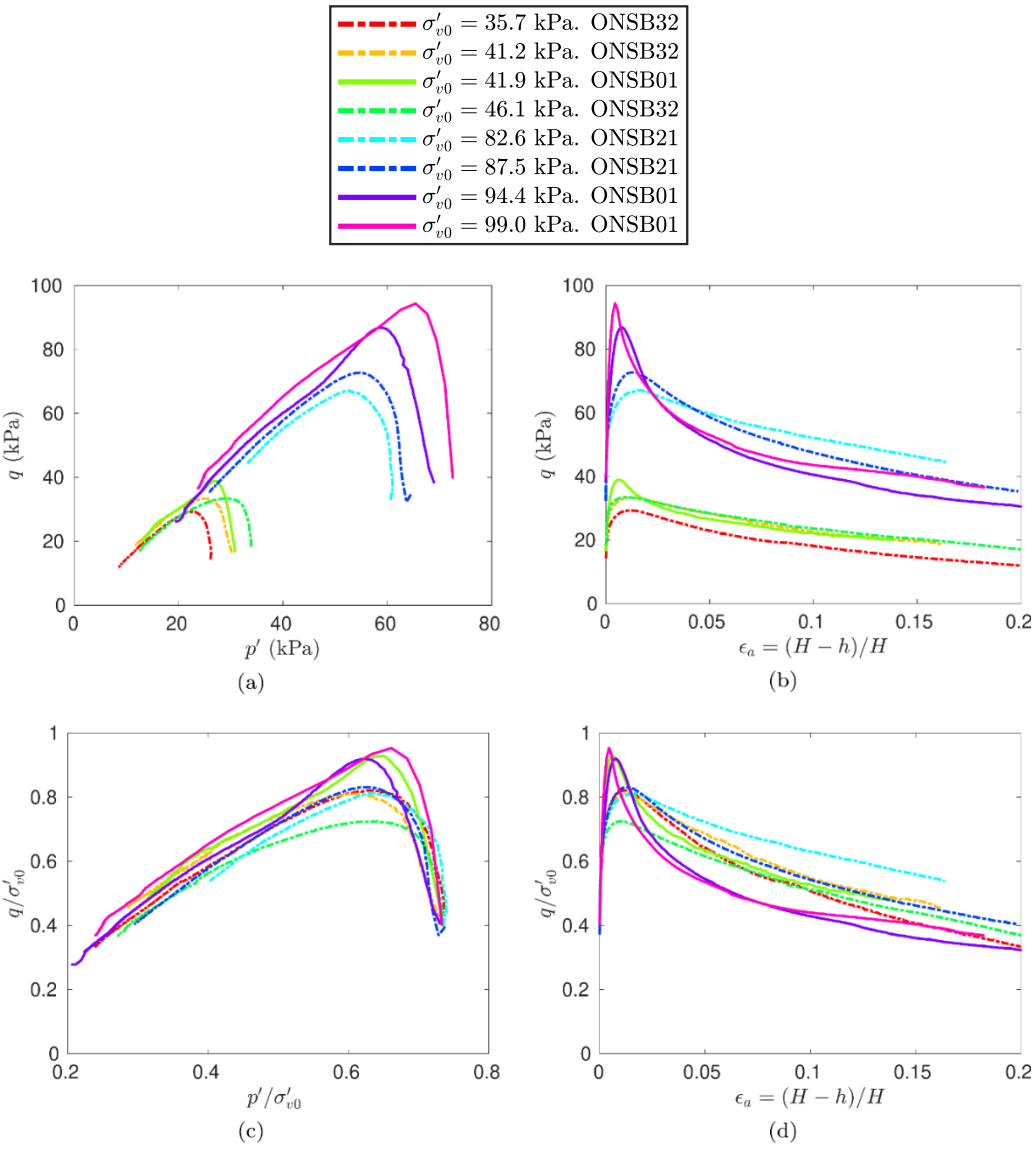

Figure 4. Onsøy site. Undrained triaxial tests on samples of excellent quality (Category 1) according to [21] methodology. Results from block samples are depicted with a continuous line.

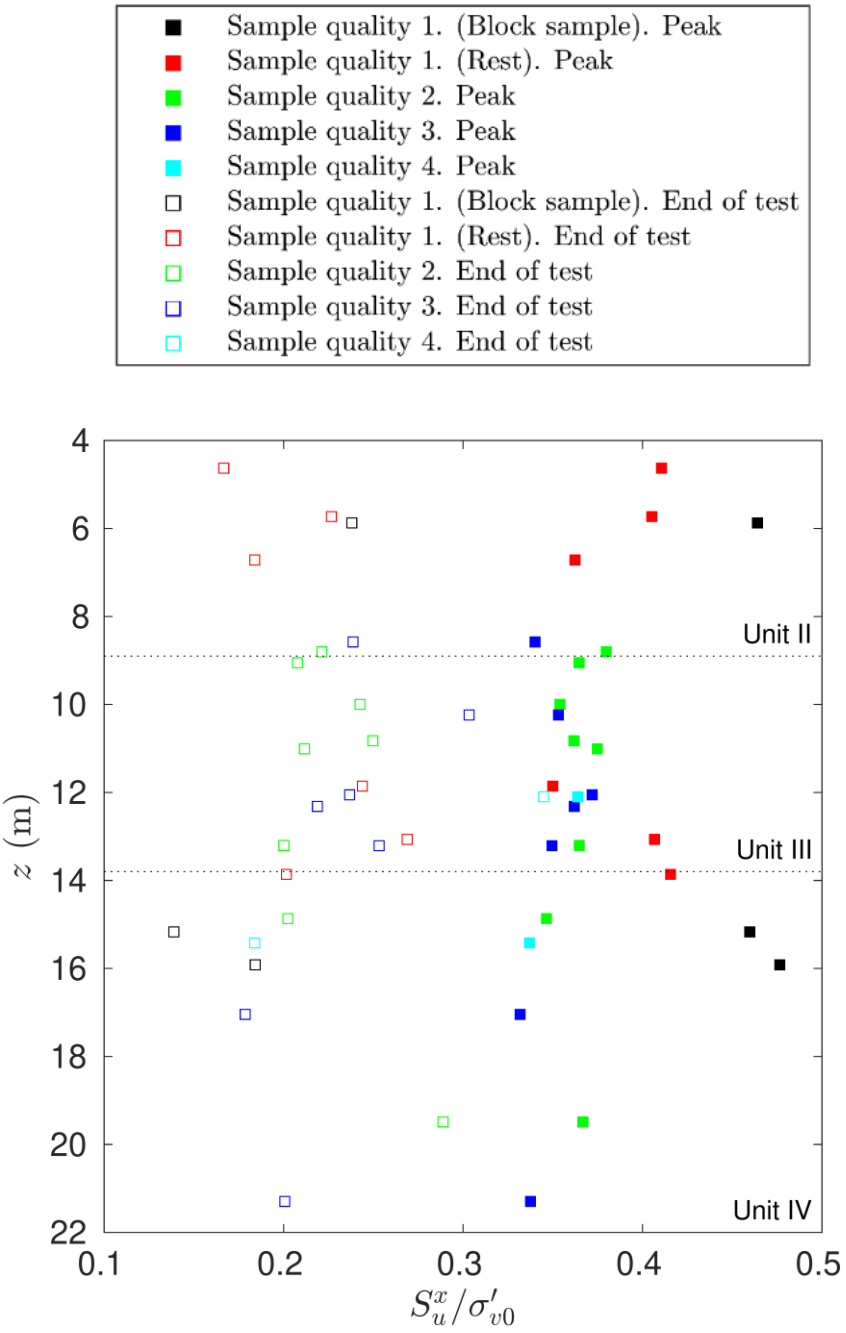

Figure 5. Onsøy site. Peak and end-of-the-test undrained shear resistance in terms of depth and sample quality.

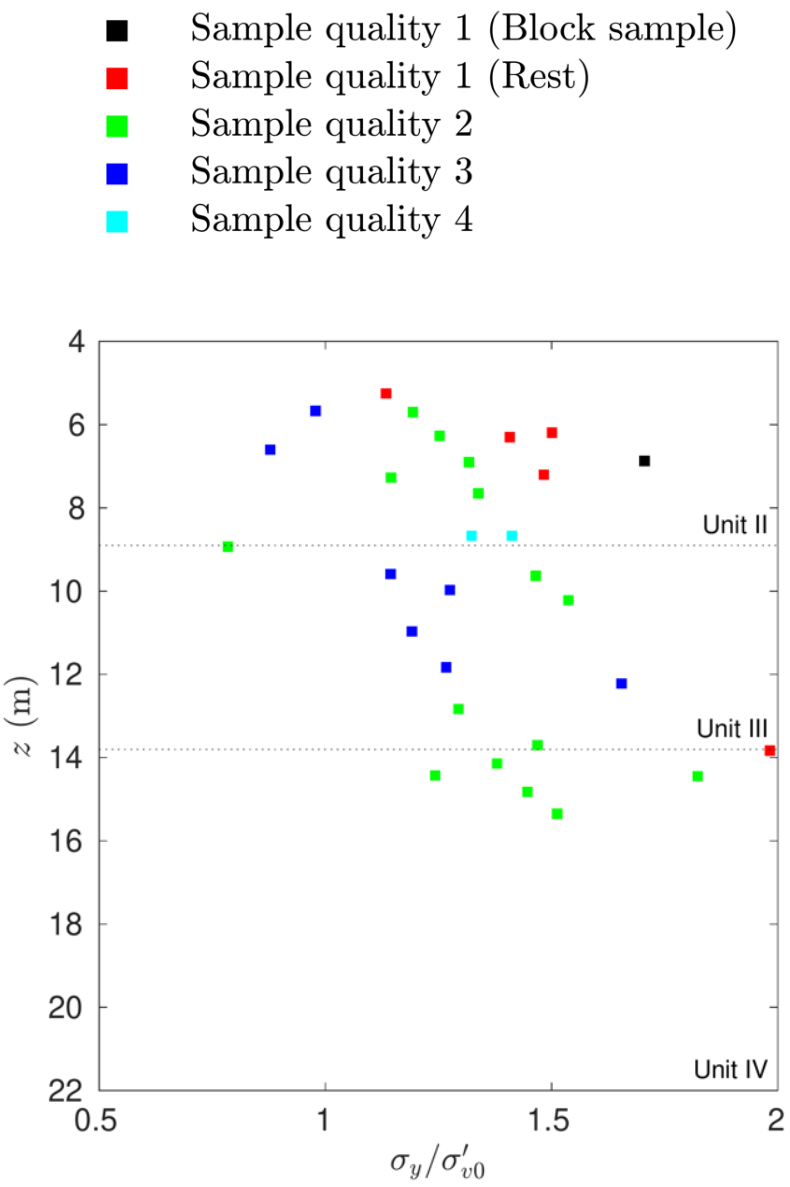

Figure 6. Onsøy site. Yield stress ratio measured in oedometric testsof the CPTu test area.

2.1.3. CPTu

The CPTu tests considered were performed during September 2017. The initial focus of this CPTu campaign was on test repeatability [23], but the results also enable us to gauge the spatial variability of the site. The campaign included 5 different test series, in which cones from different manufacturers were pushed with different equipment, although in principle all of them were compliant with available standards at the time [14,15].

All CPTu tests were carried out in an area of 10m × 10m. Figure 2 shows the test locations; each campaign is represented by a different color and, following [15], each of the CPTu manufacturers is denoted by an integer number. All CPTu measurements are corrected for zero reading, the effect of temperature on the device, and cone inclination.

Figure 7(a) illustrates the test results. There is significant variability. Overall, the results of the u_2 pore water pressure seem the most repeatable across investigation points and equipment, whereas friction sleeve resistance is the most manufacturer-dependent measurement. As for the tip resistance, there seems to be a positive bias for Type 5 measurements.

Figure 7(b) presents four normalized cone metrics, the normalized cone tip resistance,

$$Q_t = \frac{q_t - \sigma_{v0}}{\sigma'_{v0}} \tag{1}$$

the normalized excess pore pressure,

$$U_2 = \frac{u_2 - u_0}{\sigma'_{v0}} = B_q Q_t \tag{2}$$

the normalized friction sleeve resistance,

$$\frac{f_s}{\sigma'_{v0}} = 100\, F_r Q_t \tag{3}$$

and the normalized effective cone tip resistance,

$$\frac{q_t - u_2}{\sigma'_{v0}} = Q_t\left(1 - B_q\right) + 1 \tag{4}$$

where σ_{v0} is the in-situ total vertical stress, σ'_{v0} the in-situ effective vertical stress and u_0 the in-situ pore pressure. The friction ratio, F_r, and the excess pore pressure ratio, B_q, are implicitly defined in the previous equations.

The normalized cone tip resistance appears very similar for all cones except, again, for cone type 5. It is also evident that this metric does not show a strong trend with depth, once it is past the desiccation crust. Normalized excess pore pressure does not show any trend with depth either. Normalized friction sleeve resistance decreases with depth, somewhat swamped by manufacturer variability. Figure 8 reports histograms of normalized cone metrics for each type of manufacturer. To increase the legibility of these histograms, a Johnson distribution function [24] was fitted to the histograms. Thus, it becomes apparent that normalized cone tip resistance is much larger for cone type 5 than the other cone types. This behavior is attributed to systematic measurement error of the cone tip resistance, and type 5 measurements will not be further considered in the remainder of this work.

The normalized excess pore pressure distributions are more repeatable, even for cone type 5. Finally, the probability distribution function of the normalized friction sleeve resistance is highly dependent on cone type. This fact can be attributed to a variety of causes [23]: (i) No correction for water pressure has been applied to the friction sleeve resistance; (ii) the values of f_s are low, between 5 to 25 kPa, near the resolution of the sensor; and (iii) the dimensions, tolerances, and roughness of the sleeves vary across manufacturers.

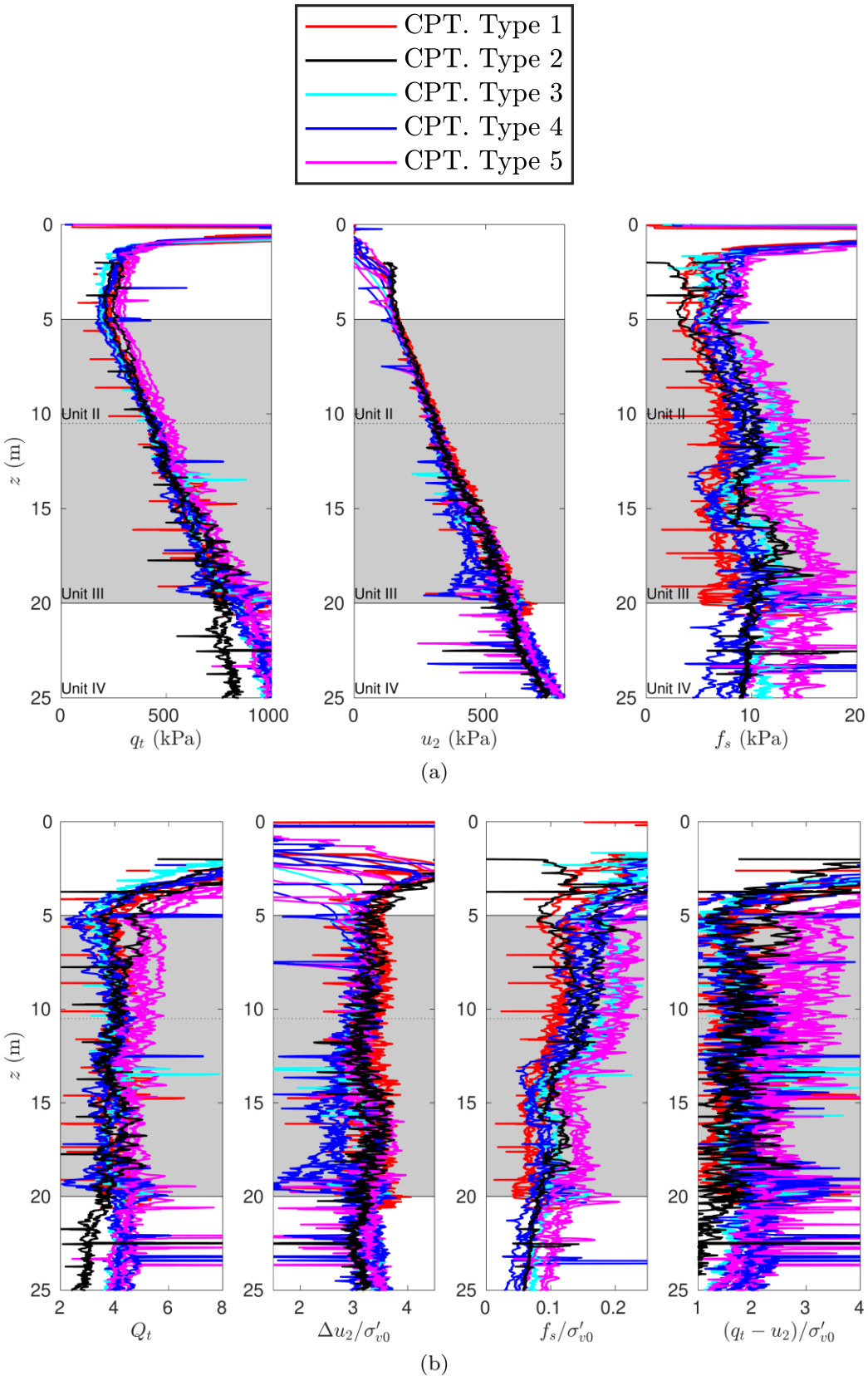

Figure 7. Onsøy site. CPTu results. Non-normalized metrics (top) and normalized metrics (bottom).

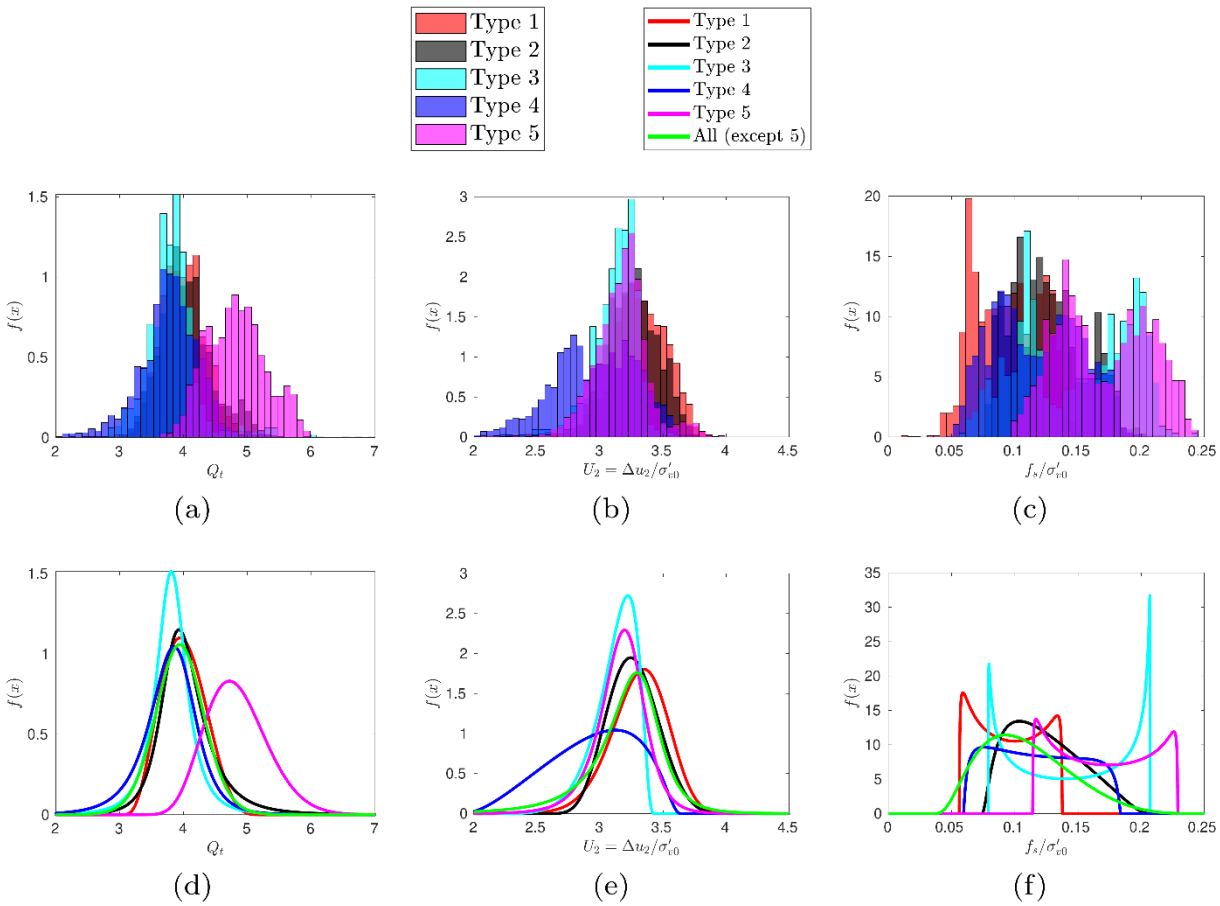

Figure 8. Onsøy site. Histograms of cone metrics in terms of the cone type (first row). Fitted Johnson's distribution to the sample distribution (bottom row).

2.1.4. DMT

We consider three DMT soundings (ONSD02, ONSD03, and ONSD04) performed at the Onsøy site in June 2022 [14]. These soundings are very close to each other, on the vicinity of the CPTu examined above (see Figure 2). They include Medusa (S)DMT tests, using standard and non-standard test protocols [17,19,20].

Figure 9 compares the three DMT readings. Good repeatability was observed, particularly for the p_1 and p_2 readings; the p_0 value was slightly higher for ONSD04. The p_0 value for ONSD04 was acquired while penetrating, with stops for other measurements only every 1 m. It seems apparent that the measurements acquired while pushing the instrument are slightly above those obtained during stoppage periods (the regular drops in the graph), which are better aligned with those from the other probes. This difference might be due to rate effects, which are known to be present in the Onsøy clay (see the Discussion section below).

Derived parameters are plotted in Figure 10. They include the horizontal stress index

$$K_D = \frac{p_0 - u_0}{\sigma'_{v0}} \tag{5}$$

the material index,

$$I_D = \frac{p_1 - p_0}{p_0 - u_0} \tag{6}$$

the dilatometer modulus,

$$E_D = 34.7\,(p_1 - p_0) \tag{7}$$

and the pore pressure index,

$$U_D = \frac{p_2 - u_0}{p_0 - u_0} \tag{8}$$

All derived parameters show good repeatability, although the higher p_0 value in ONSD04 shows a higher horizontal stress index, slightly lower material index, dilatometer modulus, and pore pressure index. All parameters appear uniform with depth except for the dilatometer modulus, which increases with depth, as expected.

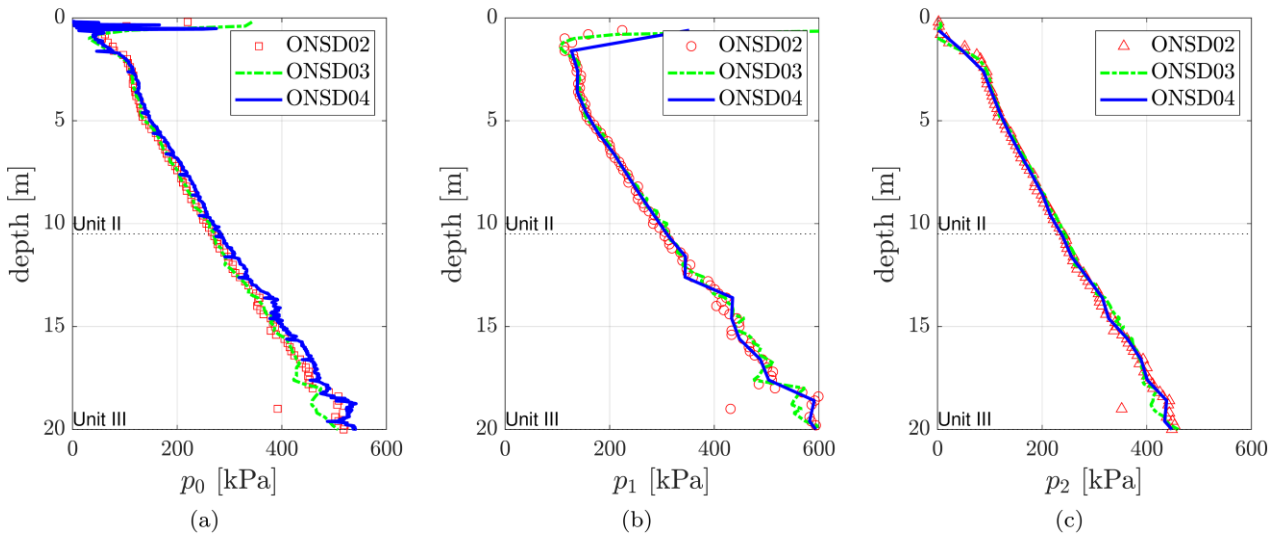

Figure 9. Onsøy site. DMT measurements.

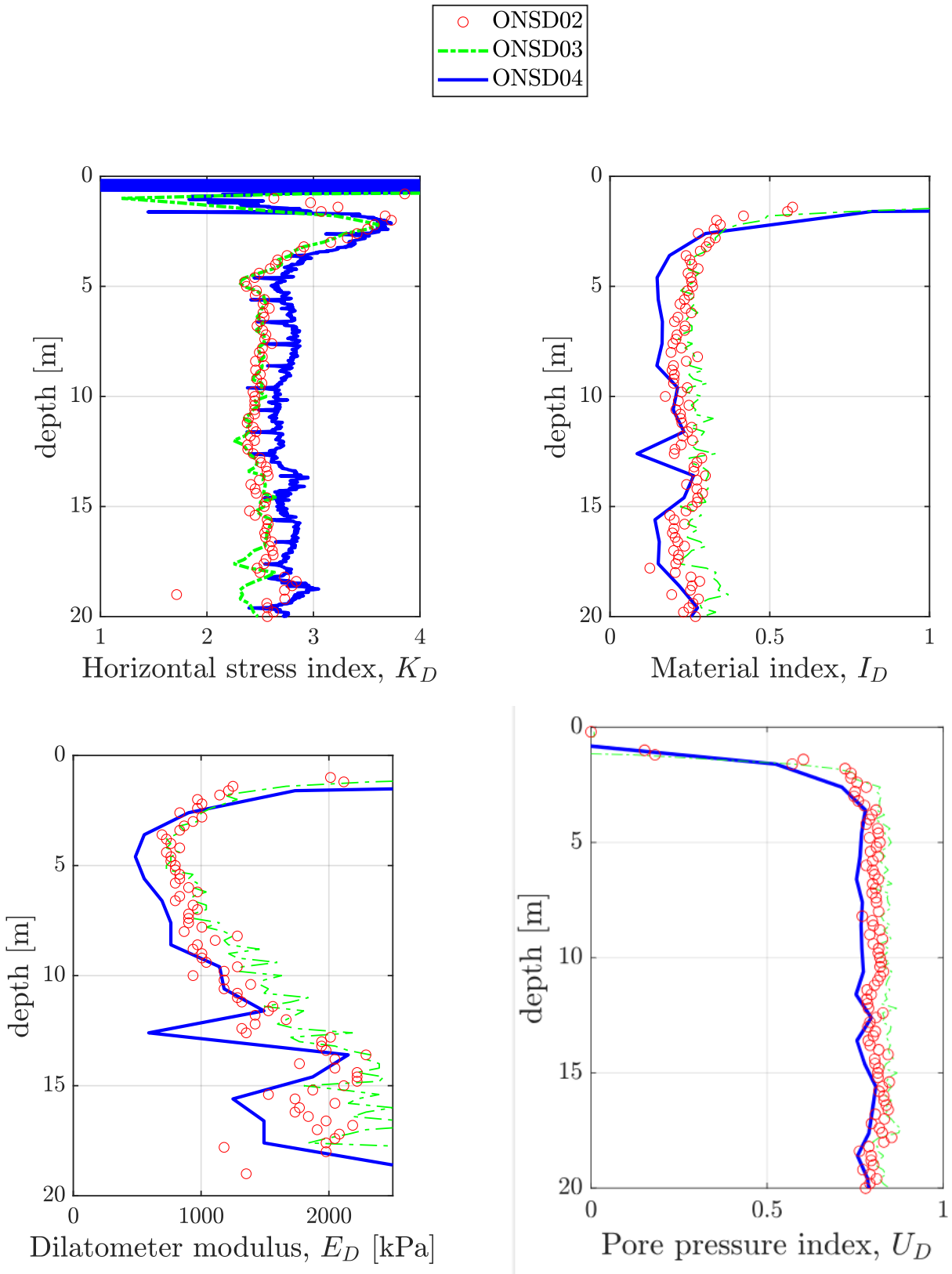

Figure 10. Onsøy site. Derived DMT parameters.

2.1.5. Comparing CPTu and DMT repeatability

It is well known that DMT results are more repeatable than those of CPTu. This has implications for the interpreted test results. Figure 11 presents normalized metrics obtained from two CPTu (ONSC07 and ONSC08) performed with the same equipment in close proximity (at a distance of approximately 1.5 m), alongside the results of two DMT for which the test protocol was similar (ONSD02 and ONSD03).

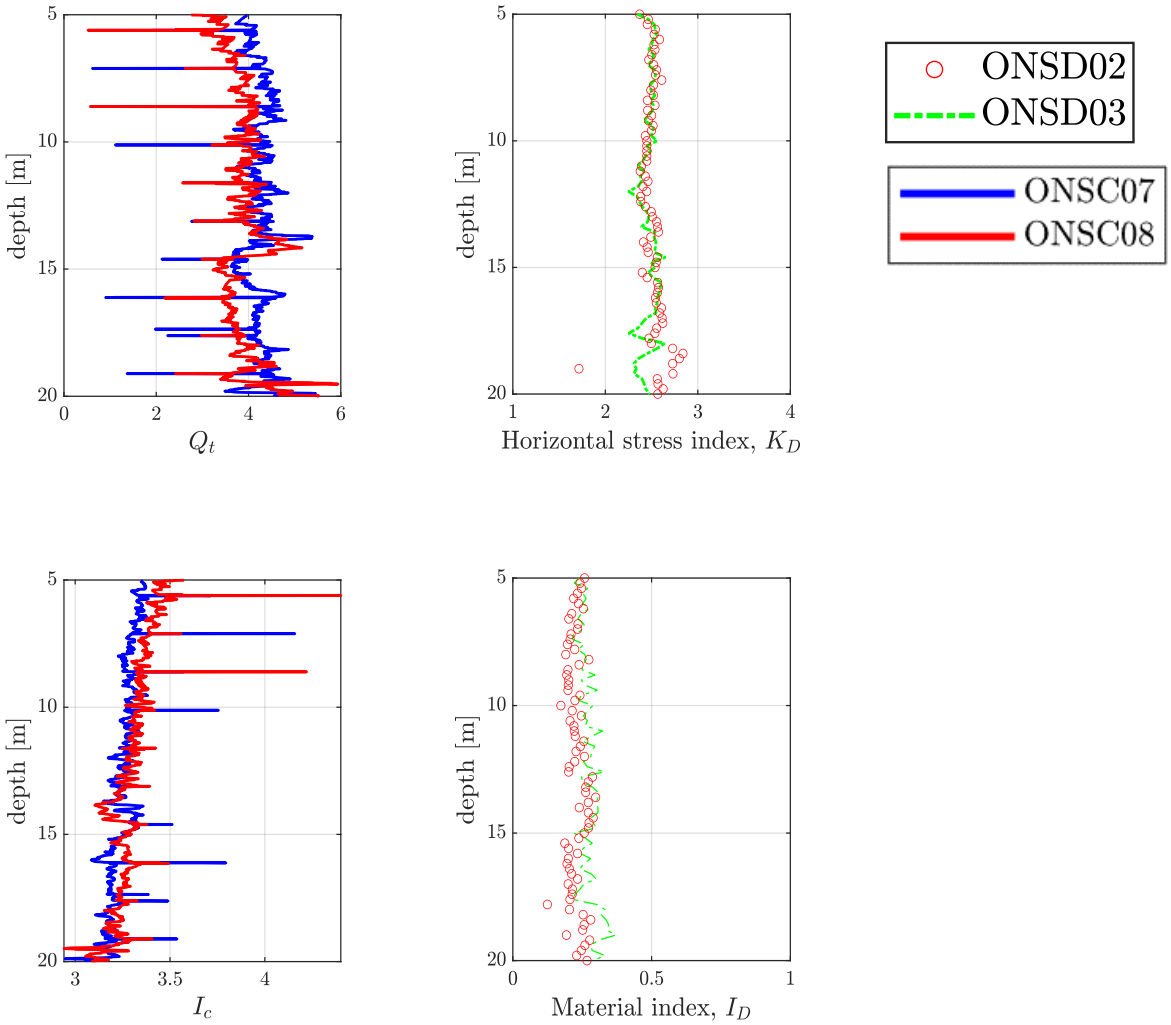

Figure 11. Onsøy site. Comparison of some DMT and CPTu normalized metrics.

We compare a normalized stress variable (the normalized cone tip resistance and the horizontal stress index) and one variable informative of material behavior, the soil behavior type index, I_c, and the DMT material index, I_D. The former is defined as:

$$I_c = [(3.47 - \log_{10} Q_{tn})^2 + (\log_{10} F_r + 1.22)^2]^{0.5} \quad (9)$$

where for clay-like materials, $Q_{tn} = Q_t$. Even if the range of each variable is different, it is clear that

cone metrics show more variability than DMT metrics: Compare, for instance, the net cone resistance, which is different among the two CPTu, and the horizontal stress index, which shows fewer differences.

Another interesting difference is that the CPTu soil behavior type index, I_c, decreases in depth, whereas the DMT material index, I_D, is independent of depth. This is partly due to the effect of normalized friction resistance, which decreases with depth. It has long been recognized that the friction sleeve resistance is probably the least repeatable of the cone metrics, yet it is used to define the soil behavior type index.

2.2. Numerical model

2.2.1. Geotechnical Particle Finite Element (G-PFEM)

The code G-PFEM is applied in all the simulations presented below. G-PFEM was specifically developed to address large-displacement and large-strain problems in geomechanics [25,26]. G-PFEM is open-source and has been implemented in the Kratos multiphysics platform [27].

G-PFEM is based on the particle finite-element method (PFEM) [28], whose key aspects include (a) a Lagrangian description of motion, (b) continuous regeneration of finite-element meshes covering the domain, and (c) low-order finite elements to compute the solution. Interpolation algorithms project information from the old to the new mesh after remeshing. The use of low-order elements simplifies some of the meshing routines and the transfer of nodal information between meshes. A typical simulation involves the steps graphically illustrated in Figure 12.

A fully coupled hydromechanical formulation is adopted. The domain is discretized with mixed stabilized linear triangles, having as degrees of freedom the displacements, the determinant of the deformation gradient or Jacobian (i.e., volume change), and water pressure. This mixed formulation alleviates volumetric locking and, in the cone penetration problem, results in smoother cone resistance curves due to smaller oscillations of water pressure [29]. To deal with strong material non-linearities, increase robustness, and reduce computational costs, stress integration is hosted within the framework of the Implex technique (Implicit-Explicit integration scheme) [30], as extended by Monforte et al. [28] for explicit stress integration techniques at the large strain regime. To alleviate mesh-dependency of the solution due to strain-softening, a non-local regularization technique is employed [31].

The contact constraints between the soil and the structure are introduced to the solution by means of a penalty approach. In the simulations reported herein and to further simplify the numerical formulation, it is assumed that the structure can be discretized as a smooth parametric surface, whose displacements in time are known beforehand. Further details can be found elsewhere [32,33].

2.2.2. Constitutive model (C-CASM)

In this work, we use a modified version of CASM [34] extended to account for structure and destructuration [35]. This model, which we denote as C-CASM, is appropriate for monotonic loading, has the advantage of being relatively simple, and has been employed before to analyze in-situ tests [7,12], as well as geotechnical structures [36]. C-CASM has been implemented in G-PFEM in general stress space, using a large-strain elasto-plastic framework in which the deformation gradient splits

multiplicatively into an elastic and plastic part. Because of the intense softening associated with destructuration, the model is implemented using an integral-type non-local regularization [31]. For presentational purposes, the constitutive model is briefly described below in terms of stress invariants.

The yield surface is expressed as:

$$f = \left(\frac{q}{M_\theta\ (p' + p_t)}\right)^n + \frac{1}{\ln(r)}\ln\left(\frac{p' + p_t}{p_t + p_s + p_m}\right) \tag{10}$$

where p' and $q = \sqrt{3\,J_2}$ are invariants of the effective stress tensor. M_θ is the stress ratio at critical state, which varies with Lode's angle according to a smoothed Mohr-Coulomb failure criterion [37]. For triaxial compression $\theta = 30^0$ and the relation between the Mohr Coulomb friction angle and M is given by

$$M = \frac{6\sin\varphi}{(3-\sin\varphi)} \tag{11}$$

The yield surface features three stress-like state variables (Figure 13): p_s stands for the preconsolidation stress of a reference, unstructured soil. As in the Cam Clay model, a classical isotropic volumetric hardening rule governs the evolution of the preconsolidation stress:

$$\dot{p}_s = \frac{p_s}{\lambda^\star - \kappa^\star}\,\dot{\epsilon}_v^p \tag{12}$$

where $\lambda^\star = \frac{\lambda}{1+e_0}$, λ is the slope of the isotropic compression line and the critical state line in the compression plane, $\kappa^\star = \frac{\kappa}{1+e_0}$, κ is the slope of the reloading curve, and $\dot{\epsilon}_v^p$ stands for the time derivative of the plastic volumetric strains.

The model is non-associated, using a flow rule proposed by [38]. According to this rule, plastic dilatancy for triaxial compression conditions is given by:

$$d^p = \frac{m-1}{m}\frac{{M_\theta}^m - \eta^m}{\eta^{m-1}} \tag{13}$$

where m is a constitutive parameter of the model, $\eta = \frac{q}{p'}$ is the stress ratio, and d^p is the dilatancy, i.e., the ratio of incremental plastic volumetric strains and plastic deviatoric shear strains.

On the other hand, p_t and p_m stand for the increase in the yield stress along isotropic paths in tensile and compressive loading, respectively. These variables represent the effect of structure and are assumed to be proportional to preconsolidation stress through the bonding variable, b:

$$p_m = b\,p_s \tag{14}$$

$$p_t = \alpha\, b\, p_s \tag{15}$$

where α is a soil constitutive parameter. The bonding variable, b, evolves according to:

$$b = b_0 \exp\big(-(h - h_0)\big) \tag{16}$$

where b_0 is the initial value of the bonding variable. The strain-like variable h depends on volumetric and deviatoric plastic strains:

$$\mathrm{d}h = h_1 \,|\mathrm{tr}\, \boldsymbol{l}^p\,| + h_2 \sqrt{\frac{2}{3}}\, l_d^p \tag{17}$$

where h_1 and h_2 are two constitutive parameters representing the rate of degradation in terms of volumetric and deviatoric plastic strains, $\boldsymbol{l}^p$ is the spatial plastic velocity gradient and $l_d^p = \sqrt{\mathrm{dev}(\boldsymbol{l}^p) : \mathrm{dev}(\boldsymbol{l}^p)}$.

2.2.3. Geometrical model

The geometry of the DMT test is three-dimensional, as the membrane expansion occurs only on one side of the blade and is perpendicular to the penetration axis. While the dimensions of the blade and membrane are standardized, those of the steel rods employed to push the blade are not. Frequently, push rods are the same as those used for the CPT, but other solutions are also possible, e.g., the use of relatively strong rods with an outer diameter of 50 mm [39]. The connector employed in this case (Figure 14) is smoothly tapered, with a taper angle of about 7.5º.

A full 3D simulation of DMT insertion and subsequent expansion is a computationally demanding problem. Butlanska et al. [40] attempted a 3D simulation using the discrete element method (DEM), but the resolution of the employed elements was not fine enough to correctly capture expansion curves. Kouretzis et al. [41] presented some quasi-3D results for penetration, imposing plane strain in the membrane plane and ignoring rod geometry. Most other attempts to date have imposed greater simplifications using cavity expansion analogues [42] or plane strain or axisymmetric conditions [43]. Following a similar approach and emphasizing the effect of the pushing rods during the instrument advance into the ground, [11] examined the performance of different plane strain and axisymmetric analogue geometries for DMT advancements in the case of non-structured clays. It was concluded that the virtual blade geometry illustrated in Figure 15 offered a good approximation to measurements of lift-off DMT pressure p_0.

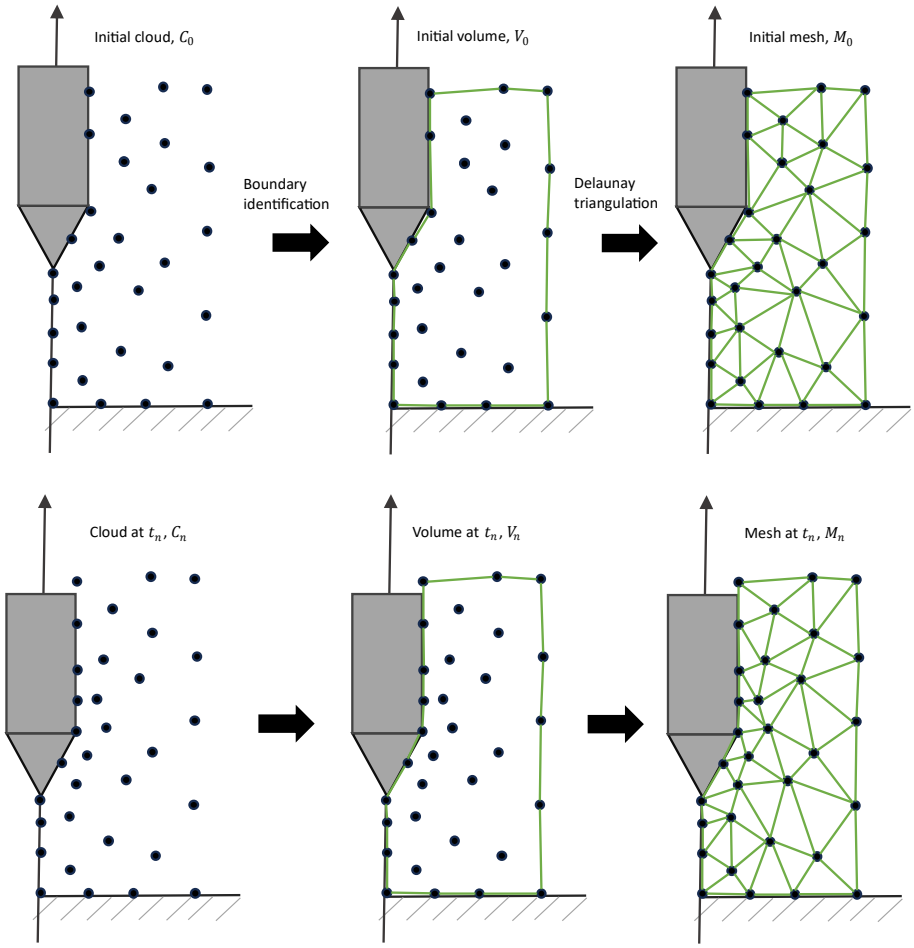

Figure 12. G-PFEM: Sequence of steps to update in time a cloud of nodes presenting a soil mass that is progressively deformed due to the penetration of a rigid object.

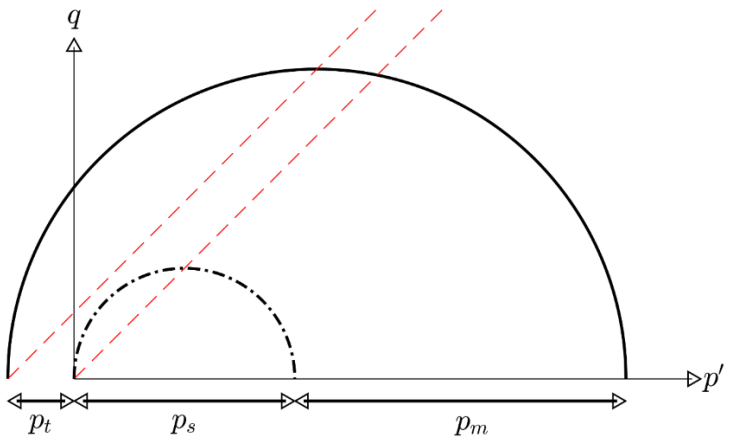

Figure 13. CASM with structure: Sketch of the yield surface in the $p' - q$ plane for triaxial conditions.

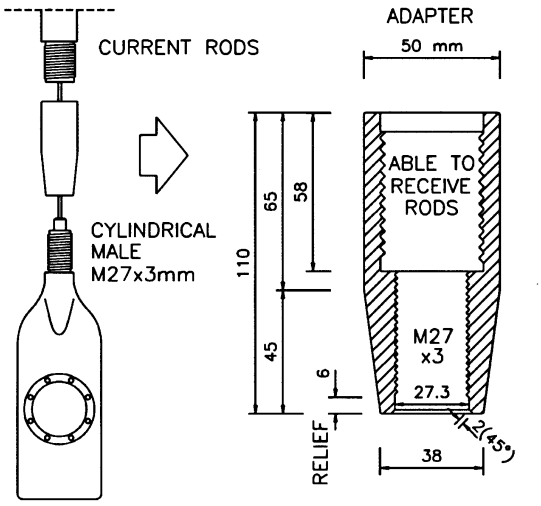

Figure 14. Typical connector section [39].

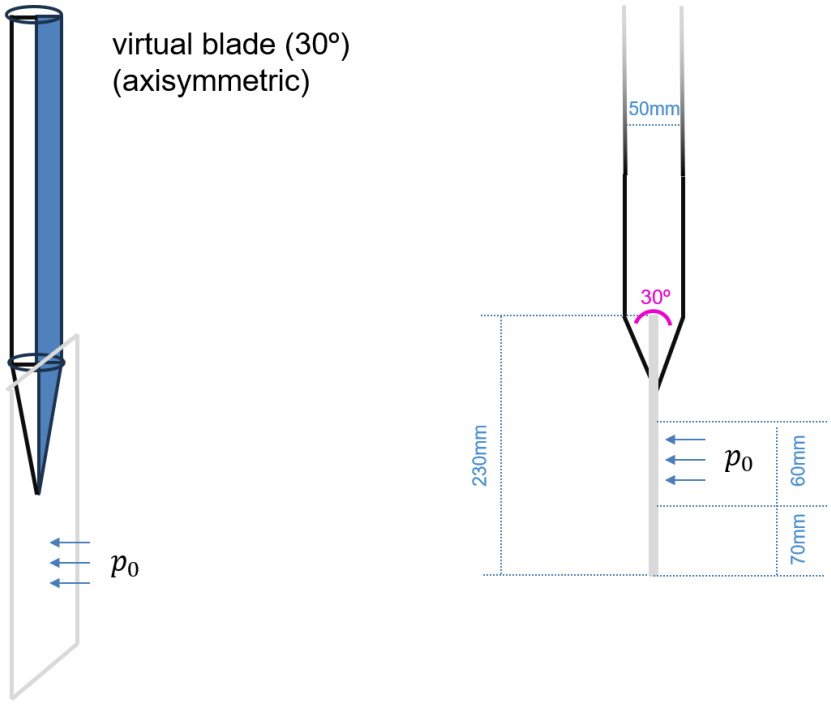

Figure 15. Detailed geometry of the virtual blade under a 30º conical tip rod.

3. Results

3.1. Calibration strategy

Ideally, we would like to calibrate the model based only on laboratory data and then simulate the field tests as verification. However, this approach faces important problems in this case as a) the lab

campaign was not oriented by the constitutive model employed and some key properties (e.g., the critical state line in the compression plane) were not determined systematically, and b) sample disturbance strongly affected the results leaving the precise value of the in situ bonding variable open to interpretation.

Therefore, we employ a different methodology. We perform numerical simulations by fixing some constitutive parameters (those for which the lab results are less ambiguous and/or those that are less consequential for simulation outputs) and, through a screening parametric study, we examine the effect of those parameters that are more uncertain and/or have more impact on the simulated response.

The fixed parameters are:

- Swelling slope. $\kappa^* = 0.01$. This value is representative of stiff soils and, at Onsøy, falls within the observed range on unloading-reloading oedometric tests [14]. As a result of this choice and that of λ below, plastic and elastic volumetric stiffnesses are one order of magnitude apart, a ratio that is typical of cemented, lightly overconsolidated clays [35].
- Poisson's ratio. $\nu = 0.15$. This is a value generally adequate for initially stiff soils. In conjunction with the value of κ^*, successfully reproduces the initial load-deformation path during undrained triaxial shearing.
- Slope of the isotropic compression line (for unstructured material) and the critical state line. $\lambda^* = 0.1$. This value is also based on oedometric test results.
- Friction angle. $\phi = 34.5º$ $(M = 1.4)$. Interpreted from all undrained triaxial tests.
- Parameter controlling the tensile strength. $\alpha = 0.05$. In C-CASM, the tensile strength of the material in isotropic conditions is $\alpha\, b\, p_0$. The value of the parameter α has been assumed based on previous experience with the model.

These fixed values are used in combination with three sets of parameters, chosen to cover the likely range of some important soil responses, namely the residual undrained strength ratio, the peak undrained strength ratio, and the rate of structure degradation.

The residual undrained shear strength predicted by the constitutive model is a consequence of the assumed yield surface for the unbonded, reference yield surface, and the soil's initial stress state. In C-CASM, this is represented by the yield surface parameters n, r and the initial state variable p_s. For the Onsøy analysis, we selected five different possibilities, denoted with a letter (A, B, C…) in Table 1. They represent different yield surfaces for the unbonded, reference material. As indicated in Table 1, these 5 yield surfaces correspond to materials with residual undrained shear strength ratios ranging from $S_u^{res} = 0.07\ \sigma'_{v0}$ to $S_u^{res} = 0.19\ \sigma'_{v0}$. This range was deemed appropriate based on a) the end-of-the-test strength observed during undrained triaxial loading and b) CPTu friction sleeve values, which, in undrained conditions, approximate residual undrained shear strengths [44,45].

For a fixed yield surface and initial stress, peak undrained shear strength is controlled in C-CASM by the initial bonding value, b_0. Thus, for each yield surface, we perform simulations using six different values of initial bonding. The characteristics of these C-CASM materials are reported in Table 1, which includes both input values (yield surface parameters, initial bonding variable) and key output responses (peak and residual undrained shear ratios, Bishop brittleness index, and odometric yield stress ratio).

The materials selected for screening cover a range of peak undrained strengths going from $S_u^{peak} \approx 0.36\ \sigma'_{v0}$ to $S_u^{peak} \approx 0.56\ \sigma'_{v0}$. The lowest value corresponds to the lowest peak strength

ratio from samples of quality class 1. The largest value is higher than that observed in any element tests: This could be justified assuming that block samples were affected by some disturbance.

Table 1. Characteristics of the different C-CASM materials employed in the screening simulations.

	Yield surface			Initial state	Strength			Oed yield stress ratio
	n	r	p_s	b_0	$\frac{S_u^{peak}}{\sigma'_{v0}}$	$\frac{S_u^{res}}{\sigma'_{v0}}$	I_b	$\frac{\sigma_y}{\sigma'_{v0}}$
			(kPa)					
A	3	2.8	59.23	0.3	0.353	0.192	0.455	1.28
A	3	2.8	59.23	0.6	0.421	0.192	0.543	1.56
A	3	2.8	59.23	1	0.481	0.192	0.600	2.02
A	3	2.8	59.23	1.3	0.516	0.192	0.627	2.3
A	3	2.8	59.23	1.6	0.545	0.192	0.647	2.65
A	3	2.8	59.23	2	0.579	0.192	0.668	3.05
B	3	4	60.50	0.6	0.387	0.137	0.646	1.60
B	3	4	60.50	1	0.440	0.137	0.689	2.02
B	3	4	60.50	1.5	0.489	0.137	0.720	2.48
B	3	4	60.50	2	0.528	0.137	0.741	2.99
B	3	4	60.50	2.3	0.549	0.137	0.751	3.34
B	3	4	60.50	2.7	0.575	0.137	0.762	3.75
C	3.5	5	59.14	0.6	0.383	0.114	0.701	1.61
C	3.5	5	59.14	1	0.431	0.114	0.734	2.02
C	3.5	5	59.14	1.5	0.474	0.114	0.759	2.51
C	3.5	5	59.14	2	0.508	0.114	0.775	3.02
C	3.5	5	59.14	2.3	0.526	0.114	0.783	3.31
C	3.5	5	59.14	2.7	0.548	0.114	0.792	3.73
D	4	7.5	58.38	0.75	0.392	0.080	0.795	1.72
D	4	7.5	58.38	1	0.417	0.080	0.807	1.99
D	4	7.5	58.38	1.5	0.455	0.080	0.823	2.50
D	4	7.5	58.38	2	0.485	0.080	0.834	2.98
D	4	7.5	58.38	2.6	0.516	0.080	0.844	3.53
D	4	7.5	58.38	3	0.535	0.080	0.850	3.88
E	5	9	56.84	0.75	0.406	0.070	0.828	1.81
E	5	9	56.84	1	0.428	0.070	0.837	2.08
E	5	9	56.84	1.6	0.467	0.070	0.851	2.69
E	5	9	56.84	2.2	0.498	0.070	0.860	3.35
E	5	9	56.84	2.9	0.529	0.070	0.868	4.08
E	5	9	56.84	3.3	0.545	0.070	0.872	4.51

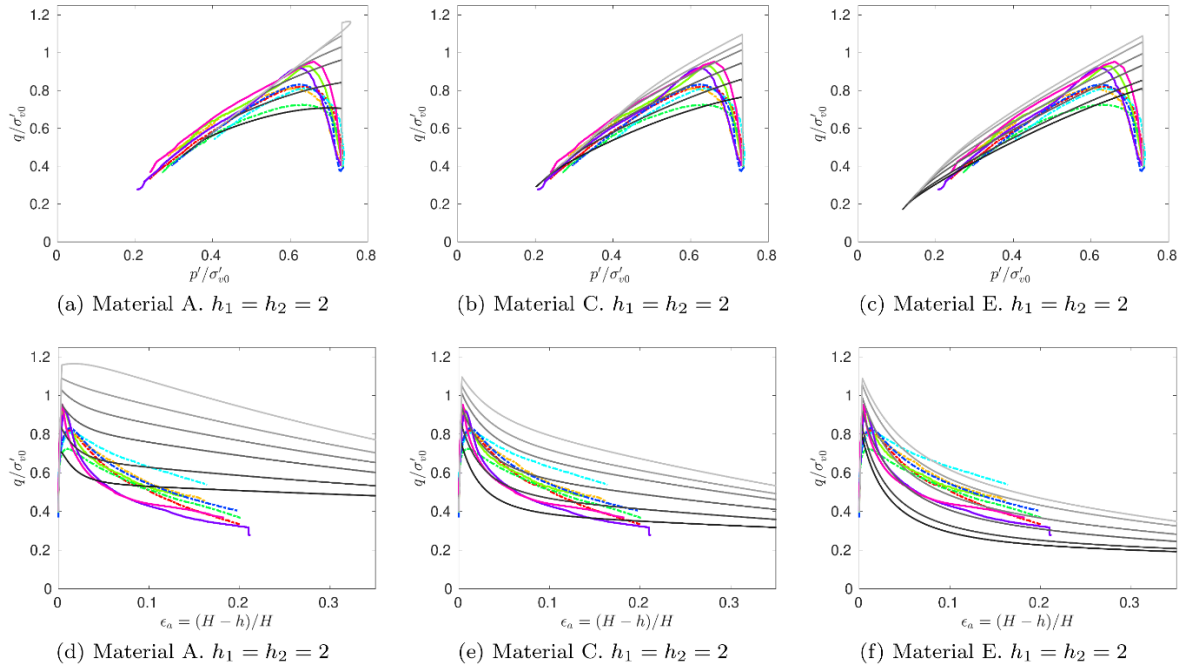

(a) Material A. $h_1 = h_2 = 2$ (b) Material C. $h_1 = h_2 = 2$ (c) Material E. $h_1 = h_2 = 2$

(d) Material A. $h_1 = h_2 = 2$ (e) Material C. $h_1 = h_2 = 2$ (f) Material E. $h_1 = h_2 = 2$

Figure 16. Onsøy site. Simulation (grey lines) for Material A (highest residual undrained shear strength), Material C, and Material E (lowest residual undrained shear strength) of undrained triaxial tests for different levels of initial bonding and slow bond strength degradation. The laboratory data (color) corresponds to samples of very good to excellent quality (Category 1) represented in Figure 4.

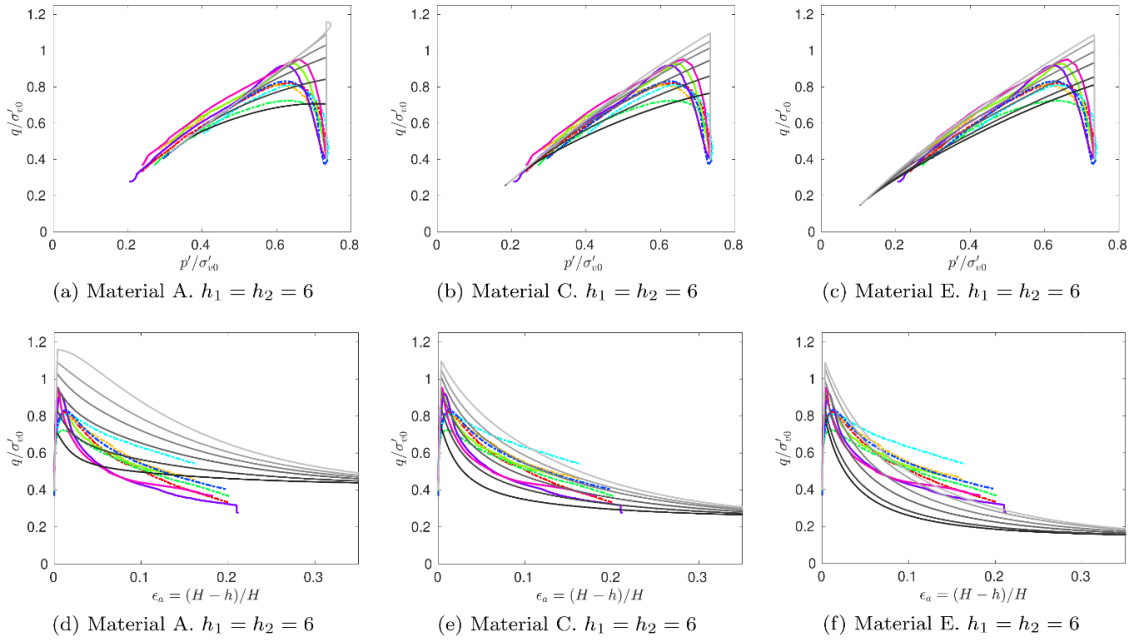

(a) Material A. $h_1 = h_2 = 6$ (b) Material C. $h_1 = h_2 = 6$ (c) Material E. $h_1 = h_2 = 6$

(d) Material A. $h_1 = h_2 = 6$ (e) Material C. $h_1 = h_2 = 6$ (f) Material E. $h_1 = h_2 = 6$

Figure 17. Onsøy site. Simulation (grey lines) for Material A (highest residual undrained shear strength), Material C, and Material E (lowest residual undrained shear strength) of undrained triaxial tests for different levels of initial bonding and fast bond strength degradation. The laboratory data (color) corresponds to samples of very good to excellent quality (Category 1) represented in Figure 4.

Finally, we also designed cases with different rates of degradation of bond-related strength. Thus, for some of the materials (shape of the yield surface and initial bonding), we have produced three simulations assigning different values to the variables controlling the rate of bond degradation: $h_1 = h_2 = 2$, $h_1 = h_2 = 4$ and $h_1 = h_2 = 6$.

To illustrate the response of the materials considered, Figure 16 and Figure 17 report undrained triaxial compression results for three materials, including Material A, with the highest residual undrained shear strength, and Material E, with the lowest. For each material, six cases are considered, with different initial bonding values. Figure 16 presents the results obtained with the lowest value of the rate of degradation of strength ($h_1 = h_2 = 2$). Figure 17 shows those obtained when those rates are at their highest values ($h_1 = h_2 = 6$). All material types (A, C, and E) have common features with some laboratory tests; however, the materials of type C with higher degradation rates perhaps show better overall similitude with the lab tests.

3.2. Numerical results: Simulations with a fixed bond degradation rate

We carried out simulations to explore the effect of the peak and residual undrained shear strength on the response recorded by the penetrating instruments while having a constant value of the parameter controlling bond degradation ($h_1 = h_2 = 2$).

The numerical results are reported in two parts. In the first part, we present results of CPTu simulations and then move to the DMT proxy. All simulations are advanced until steady state conditions are observed on the measurements. This typically occurs after 0.4 m for the cone and 0.35 m for the DMT proxies.

In all cases, the in-situ stress state is set to $\sigma'_{v0} = 76$ kPa and $\sigma'_{h0} = 45.6$ kPa ($K_0 = 0.6$), representative of site conditions at 12 m depth. Pore water pressure at this depth is $u_0 = 107.8$ kPa. In the simulations reported in this section, it has been assumed that the soil-steel interface has a friction angle of 15º.

3.2.1. CPTu

CPTu simulations were performed for all 30 cases in Table 1, including 6 values of the initial bonding variable for the 5 material types (A to E). The rate of bond degradation is the same in all cases, set at the lowest value ($h_1 = h_2 = 2$).

Figure 18 reports the normalized cone metrics obtained for each material (i.e., combination of material type and initial bonding value). As a reference, the figure includes the range of peak undrained shear strength ratios observed in undrained triaxial compression tests performed on Category 1 (very good to excellent) specimens. The figure also highlights the 25% to 75% percentile range of the corresponding distribution of field measurements.

Both normalized cone tip resistance, Q_t, and normalized pore pressure, U_2, increase clearly with peak undrained shear strength, and, for the same peak strength, with residual undrained shear strength. The excess pore pressure ratio, B_q seems fairly independent of the peak undrained shear strength but it is inversely proportional to the residual strength. Normalized effective cone tip resistance, $Q_t(1 - B_q) + 1$ and normalized side friction f_s/σ'_{v0} are also insensitive to the value of peak

undrained shear strength, but they increase with residual undrained strength.

These trends are reasonable. For instance, the normalized effective cone tip resistance has been linked to the state parameter [46,47] and, given a critical state line, the state parameter defines the residual undrained shear strength. Also, as noted above, the friction sleeve resistance measured in undrained conditions has been repeatedly shown to approximate residual undrained shear strength [44,45].

The simulation results have also been plotted in soil classification charts (Figure 19). In the Robertson chart [48], almost all results are plotted in the clay zone (zone 3) of the chart. Sensitivity (as measured by Bishop index, see Table 1) increases when going from material type A to E and, for a given material type, increases with initial bonding. That increase is correctly reflected by following the graph's expected trend. In the Schneider et al. [49] chart, all numerical results plot clusters in a very narrow region (1c), corresponding to undrained sensitive materials. Increasing peak undrained shear strength by means of initial bonding also increases yield stress and hence OCR; this agrees with the "increasing OCR" trend in the Schneider graph.

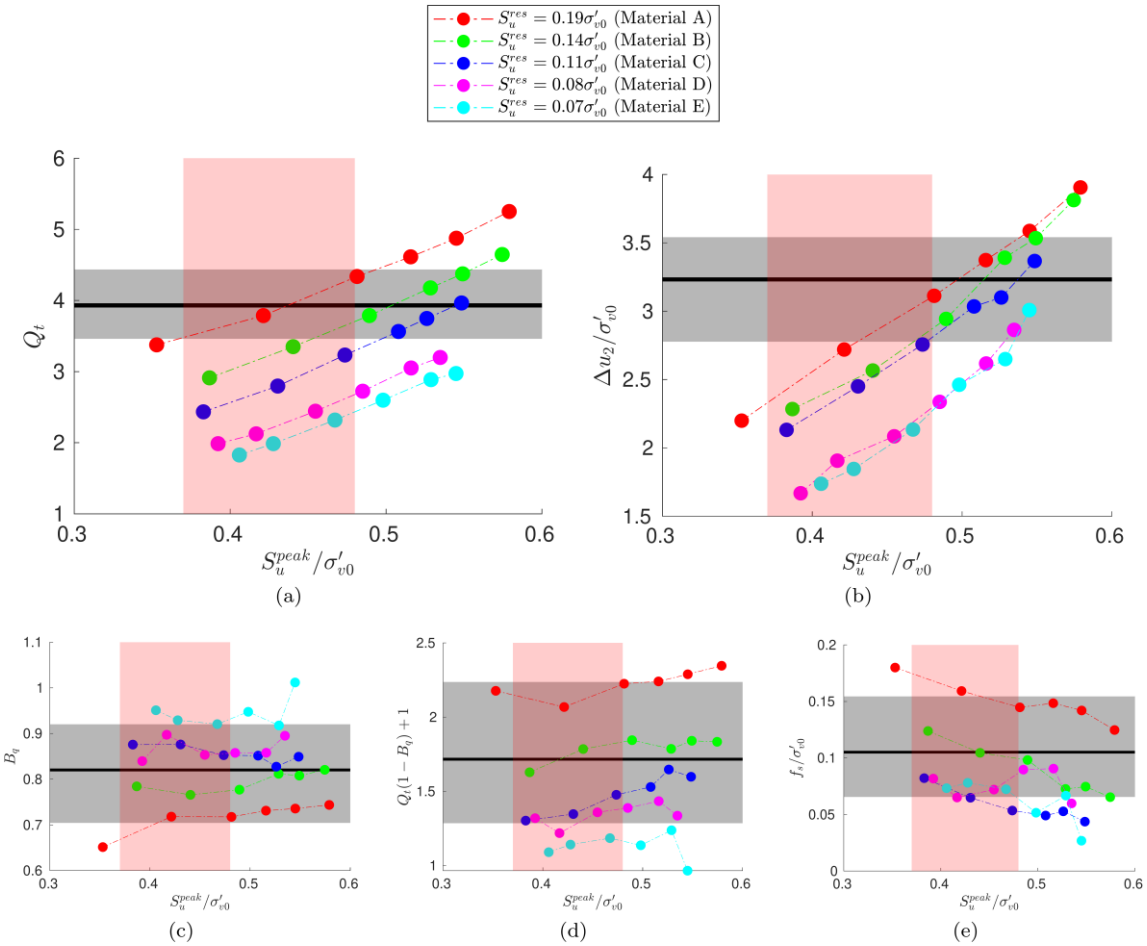

Figure 18. Onsøy site. CPTu simulations for bond degradation values fixed at ($h_1 = h_2 = 2$). Normalized cone metrics in terms of the peak and residual undrained shear strength. The pink vertical bands indicate the range of peak undrained strength observed on specimens classified as "very good to excellent" quality. The grey horizontal bands correspond to the central range (25–75%) of the observed field distributions of cone metrics. The black line indicates the mean value.

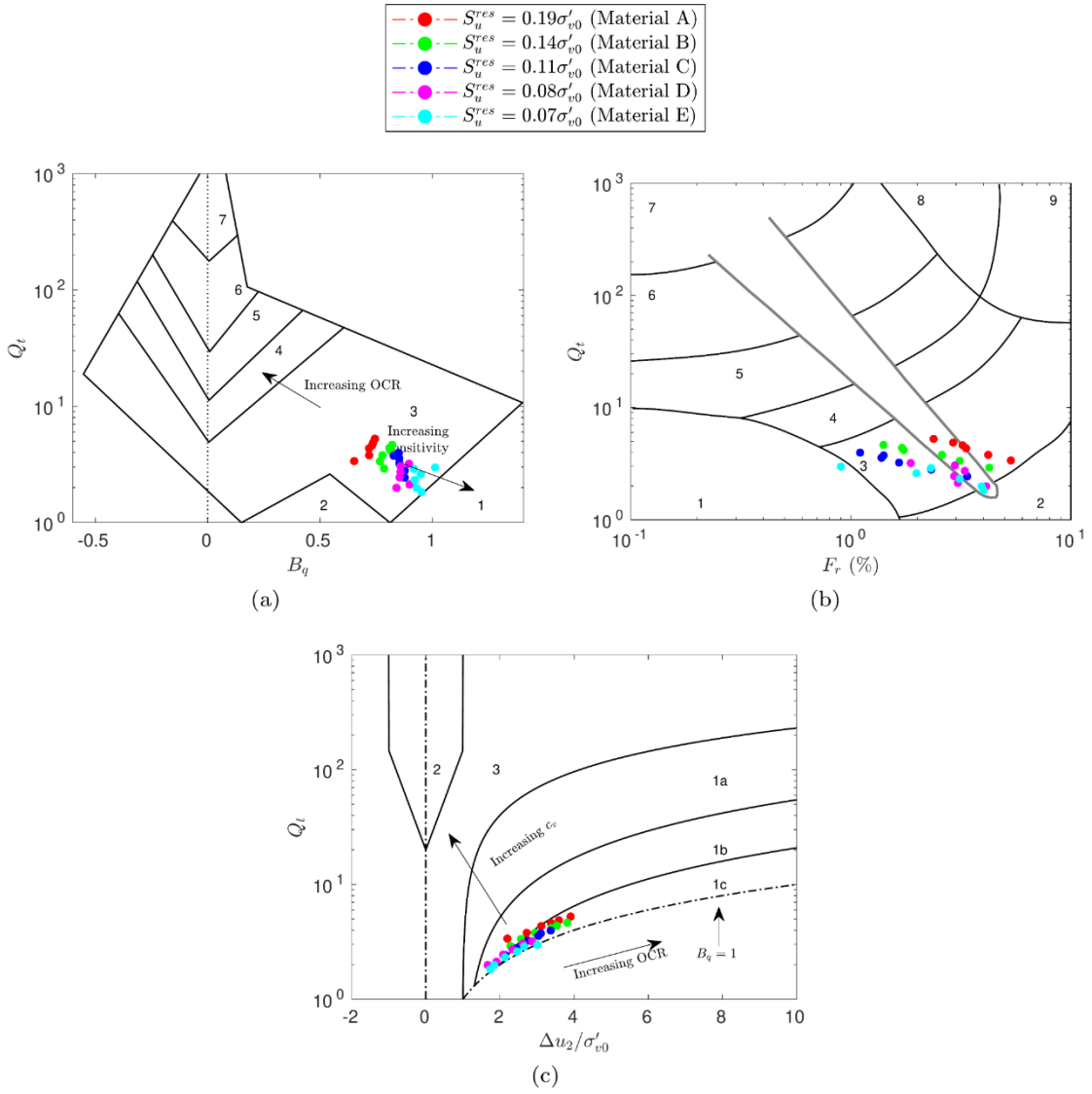

Figure 19. Onsøy site. Reference simulations. CPTu. Numerical results in interpretation charts: Robertson [48], (a), Robertson [48], (b), and Schneider et al. [49], (c).

3.2.2. DMT-proxy

Figure 20 presents the horizontal stress index, K_D predicted on the virtual blade DMT-proxy geometry for all the combinations in Table 1 of material type and peak undrained shear strength, S_u^{peak} (i.e., initial bonding). As a reference, the figure includes the range of peak undrained shear strength ratios observed in undrained triaxial compression tests performed on Category 1 (very good to excellent) specimens. The figure also highlights the 25% to 75% percentile range of the corresponding distribution of DMT K_D field measurements. Because of the better repeatability of DMT, the latter is a much narrower band than the corresponding one for the CPTu case.

For all the DMT proxy cases, the horizontal stress index depends on initial bonding (i.e., peak undrained strength), but the influence of residual undrained strength is generally small. The small

effect of residual undrained strength values on the simulated response is made evident in Figure 21, where the water pressure and total horizontal stress generated by insertion of the DMT-proxy geometry are compared for two cases with the same peak undrained shear strength and different residual undrained shear strengths. There are differences, but stresses at the membrane measurement area are very similar.

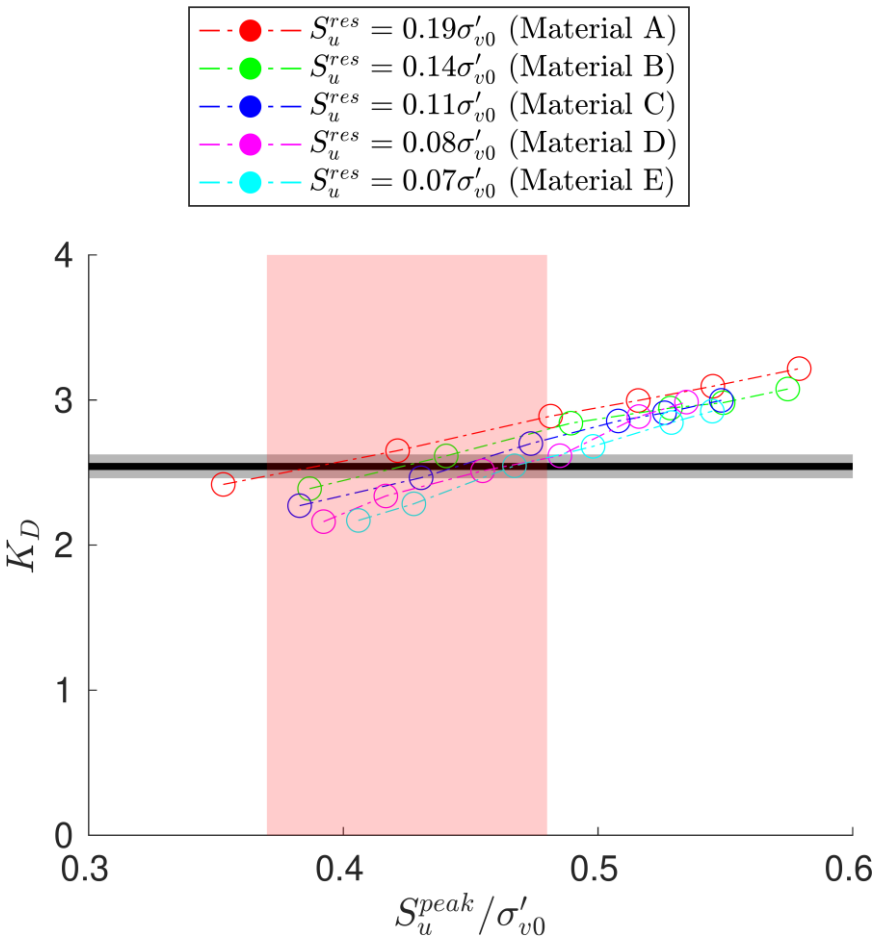

Figure 20. Onsøy site. DMT-proxy simulations for bond degradation values fixed at ($h_1 = h_2 = 2$). Horizontal stress index in terms of the peak and residual undrained shear strength. The pink vertical bands indicate the range of peak undrained strength observed on specimens classified as "very good to excellent" quality. The grey horizontal bands correspond to the central range (25–75%) of the observed field distributions of horizontal stress index. The black line indicates the mean value.

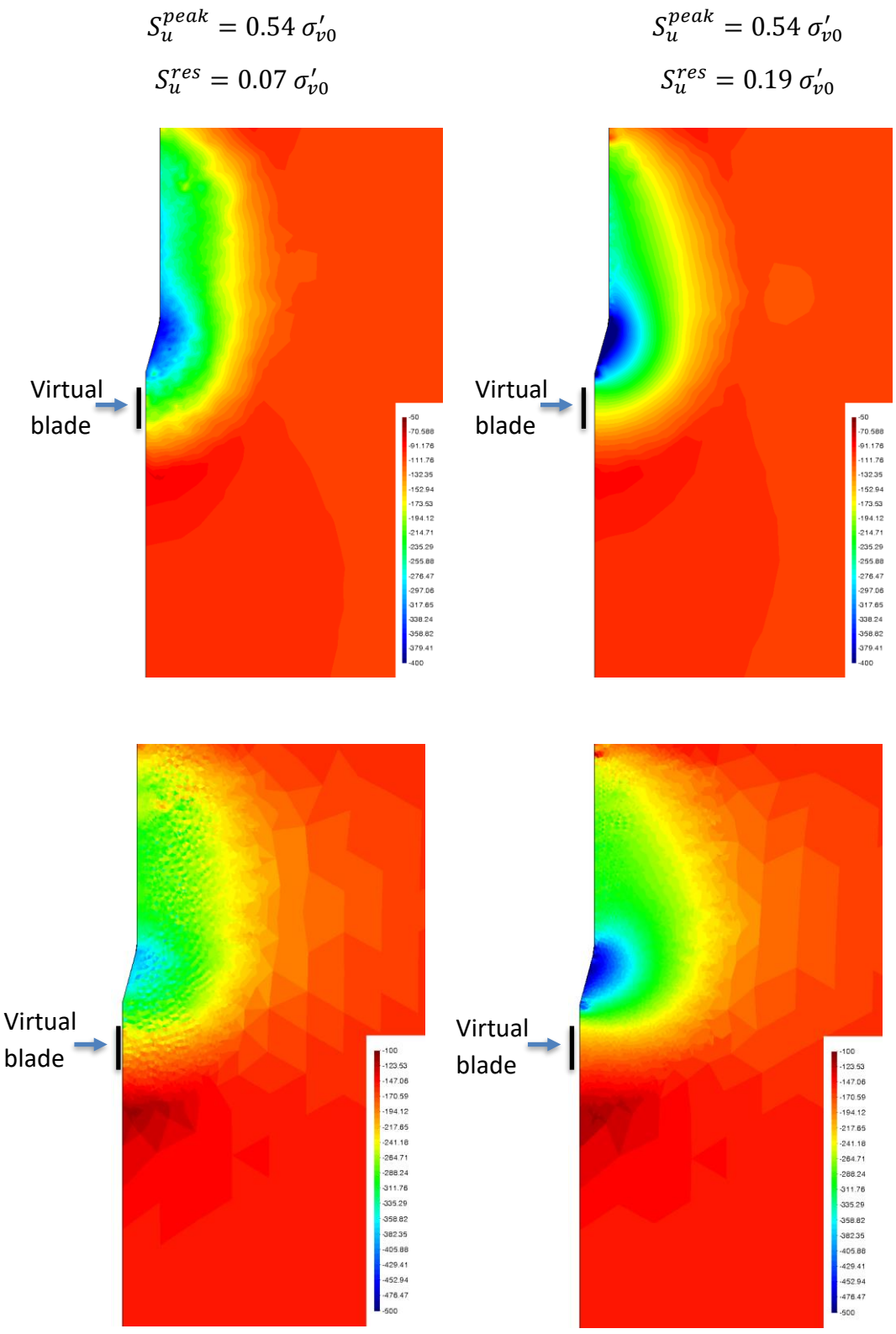

Figure 21. DMT-proxy simulations. Excess water pressure (top) and total horizontal stress (bottom).

3.3. *Numerical results: Effect of bond degradation rate*

Additional sets of simulations were run with different values of bond rate degradation parameters. For the sake of brevity, we report only results for material type A i.e., that with the highest residual undrained shear strength.

Considering first the CPTu, it is apparent that computed normalized cone resistance and normalized excess pore pressure are quite sensitive to the rate of strength degradation (Figure 22). The higher the rate of strength degradation, the lower these two normalized metrics; moreover, these differences increase for larger peak strengths. Interestingly, the rate of strength deterioration does not have much effect on the water pressure ratio, the normalized effective tip resistance, and the normalized friction sleeve resistance. As pointed out, these two last cone metrics depend only on the residual undrained shear strength; hence, they are "a priori" independent of the rate of degradation of strength from peak.

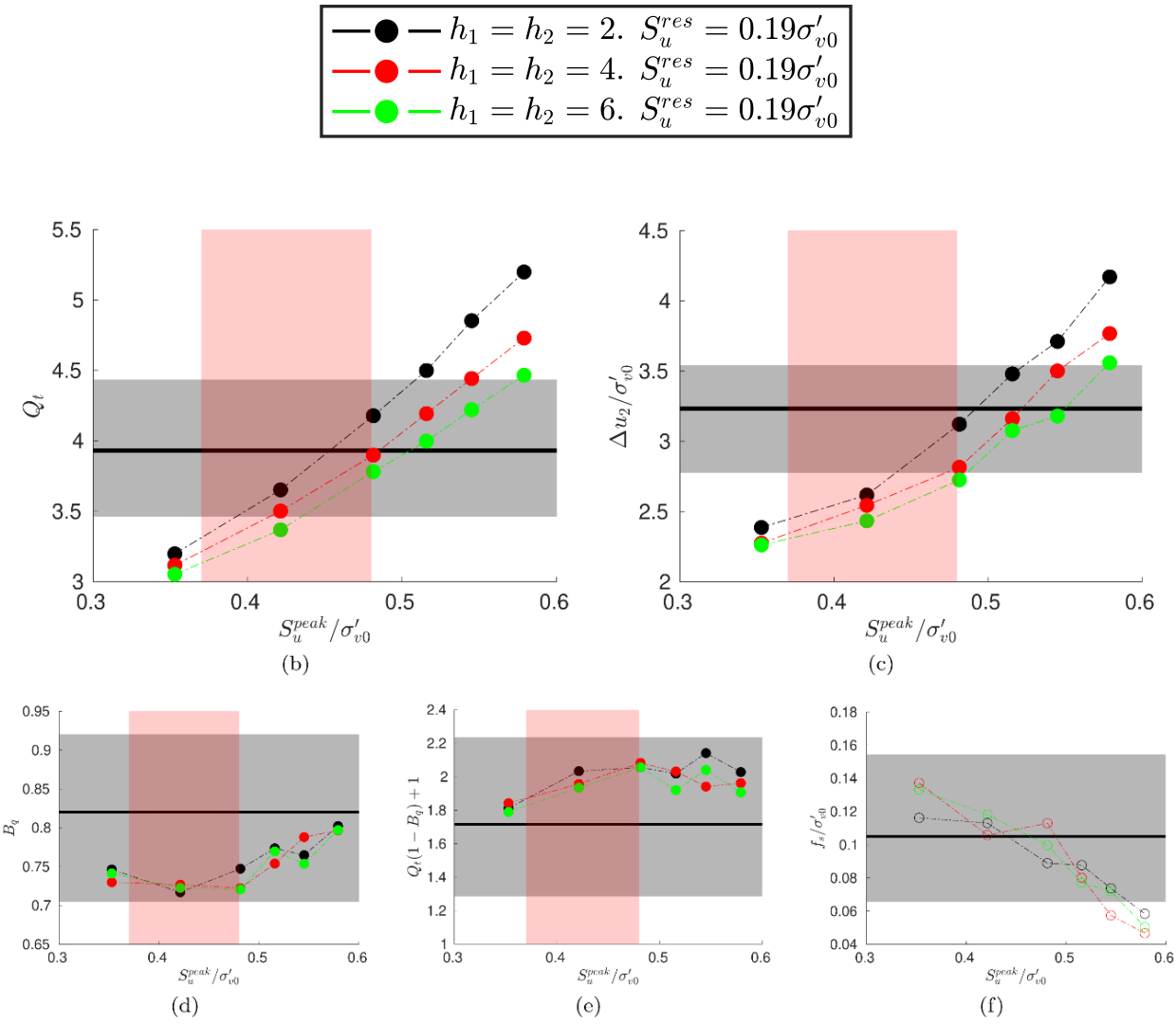

Figure 22. Onsøy site. Effect of the rate of degradation of strength. CPTu. Normalized cone metrics in terms of the peak and residual undrained shear strength.

Considering now the DMT proxy, it appears that the rate of strength degradation does not significantly impact the computed horizontal stress index (Figure 23). This result confirms that K_D is a parameter mostly controlled by the peak undrained strength ratio, where the role of undrained residual strength or strength degradation is small.

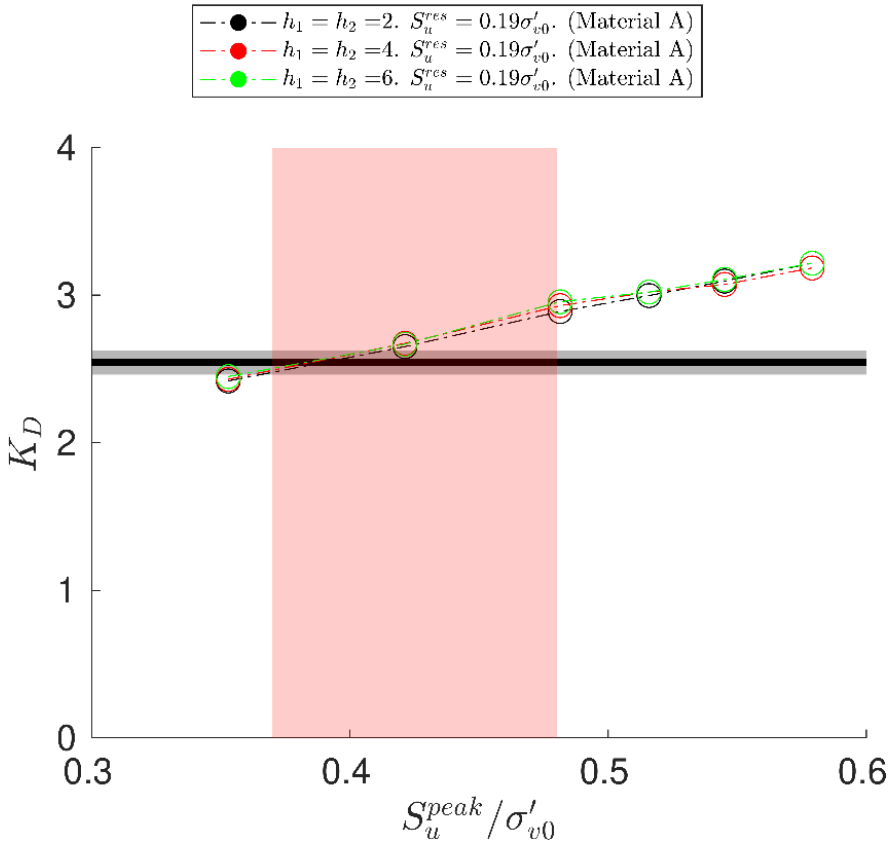

Figure 23. Onsøy site. Effect of the rate of degradation of strength. DMT-like. Numerical results in interpretation charts.

4. Discussion

4.1. Which C-CASM material is optimal for Onsøy?

Consider first the CPTu simulation results. The comparison with field and laboratory data in Figure 18 suggests that either material types A or B, with initial bonding values $b_0 < 1$, are those more likely to represent the Onsøy clay. Material A (red dots) performs better in terms of normalized tip resistance, normalized pore pressure, and normalized side friction. Material B (green dots) performs better in terms of the excess pore pressure ratio, B_q and normalized effective cone tip resistance. Overall, it is difficult to select univocally candidate materials based on the CPTu results.

Back to Figure 20 and the virtual blade DMT-proxy results, from the agreement with field measurements, we can also infer that the highest values of initial bonding are unrealistic, whatever the material type. This was elaborated further. By selecting the points that overlap the intersection of the two experimentally-based color bands in the plot of Figure 20 (the vertical band deduced from lab tests

and the horizontal band from the DMT results) we obtain a best estimate of which C-CASM materials are more likely to correctly represent the Onsøy clay. The selections obtained are presented in Table 2.

It is useful, at this stage, to consider also the yield stress ratios that were measured in the laboratory (Figure 6). When testing samples of the highest quality, the yield stress ratio is generally in the range 1.5 to 2. This would exclude the last two rows of Table 2. Of the remaining possibilities, material C (with $b_0 = 1$) has the advantage of being somewhat more consistent with the triaxial results (Figure 17). That will be the simulation-aided best estimate of C-CASM model parameters for Onsøy.

Table 2. Simulation cases that recover more realistic K_D values. Virtual Blade (30º).

	Yield surface			Initial state	Strength		State	
	n	r	p_s	b_0	$\frac{S_u^{peak}}{\sigma'_{v0}}$	$\frac{S_u^{res}}{\sigma'_{v0}}$	I_b	$\frac{\sigma_y}{\sigma'_{v0}}$
			(kPa)					
A	3	2.8	59.23	0.6	0.421	0.192	0.543	1.56
B	3	4	60.50	1	0.440	0.137	0.689	2.02
C	3.5	5	59.14	1	0.431	0.114	0.734	2.02
D	4	7.5	58.38	1.5	0.455	0.080	0.823	2.50
E	5	9	56.84	1.6	0.467	0.070	0.851	2.69

4.2. Rate effects

Rate effects are present in Onsøy clay. For instance, [50] report 8–14% increases for laboratory measurements of undrained strength as a result of order-of-magnitude changes on the strain rate applied during triaxial compression. On the other hand, [51], who carried out CPTu in Onsøy at three advance rates (0.2, 2 and 10 cm/s), observed a smaller effect of rate variation on CPTu results, with some impact on tip resistance (5–10% reduction at the slower rate; no change at the faster rate) and no change on pore pressure. There are no similar systematic results for the DMT, but the difference in p_0 values between the continuous push test and the standard procedure noted above (Figure 9) might be due to rate effects.

C-CASM is a rate-independent constitutive model, and those effects could not be explored in the simulations presented here. A separate extension of CASM that incorporates rate effects through a viscoplastic formulation is CASM-Visco. Using also G-PFEM, CASM-Visco was employed by [52] to investigate the effect of cone advance rate on the undrained response recorded by CPTu. Interestingly, they also noted that order-of-magnitude changes in cone advance rate had no effect on pore pressure measurements, but resulted in about 8–10% increases on tip resistance per order-of-magnitude.

Despite the significance of rate effects, it is clear that it is the presence of structure and consequent destructuration that has a larger impact on geotechnical engineering of Onsøy clay. It would thus be desirable to consider rate effects in combination with structure effects. The combined effect of structure and rate effects on natural clays has been incorporated in more advanced constitutive models (e.g., [53]). Such models may be incorporated into G-PFEM or similar tools in the future for a more comprehensive simulation of "in situ" test results.

5. Conclusions

We set out to demonstrate the benefits of a systematic approach to geotechnical characterization in which parallel simulations of laboratory and "in situ" test results are exploited to calibrate realistic but relatively complex constitutive models. This general concept was illustrated with the calibration of a structured elasto-plastic soil model (C-CASM) to represent the mechanical behavior of Onsøy clay, a naturally structured soft marine clay. Onsøy clay is very brittle and therefore very difficult to sample intact; as a result, a laboratory-only approach to model calibration is hampered by the induced artefacts derived from sampling-induced damage.

The simulation of in-situ tests was made possible using the advanced numerical technology built into the code G-PFEM. It was highly beneficial for this strategy to represent not just CPTu but also, even if through a geometrical proxy, DMT insertion and the relevant lift-off pressure. DMT field data showed less measurement variability than CPTu, which was advantageous for calibration. Moreover, it was advantageous and an interesting outcome of the analysis that the horizontal stress index of DMT, K_D, showed a strong dependency on the peak undrained shear strength but was almost insensitive to the residual undrained shear strength and the rate of structure degradation. The methodology demonstrated here may be of use in the calibration of constitutive models for other natural structured clays and, more generally, in the characterization of soils for applications in which numerical analyses plays a significant role.

Author contributions

Lluís Monforte: Software, Visualization, Investigation, Writing–Original Draft Preparation, Writing–Review & Editing. Laurin Hauser: Software, Visualization, Investigation, Writing–Review & Editing. Paola Monaco: Investigation, Data Curation, Writing–Review & Editing Anna Chiaradonna: Investigation, Data Curation, Writing–Review & Editing. Sara Amoroso: Investigation, Data Curation, Writing–Review & Editing. Marcos Arroyo: Conceptualization, Investigation, Writing–Original Draft Preparation, Writing–Review & Editing. Diego Marchetti: Conceptualization, Investigation, Writing–Review & Editing.

Acknowledgments

DMT test data at Onsøy were obtained as part of the Transnational Access project JELLYFISh funded by Horizon 2020-GEOLAB (Grant Agreement No. 101006512). The remaining experimental data were obtained as part of the NGTS - Norwegian Geo-Test Sites project and are publicly available online; the authors express their gratitude to NGTS team for making the data accessible. Support from the Spanish Ministry of Science, Innovation and Universities (MICIU/AEI/10.13039/501100011033) and the European Union (ERDF/EU) through project MODEST (PID2023-149935OB-I00) is also gratefully acknowledged.

Use of AI tools declaration

The authors declare they have not used Artificial Intelligence (AI) tools in the creation of this article.

Conflict of interest

The authors have no conflict of interest

References

1. Tan TS (2003) *Characterisation and engineering properties of natural soils*, CRC press
2. Tan TS, Phoon KK, Hight DW, et al. (2006) Characterisation and Engineering Properties of Natural Soils, *Proceedings of the Second International Workshop on Characterisation and Engineering Properties of Natural Soils*, Singapore. CRC Press.
3. Gens A (1993) Conceptual bases for a constitutive model for bonded soils and weak rocks. *Geotech Eng Hard Soils-Soft Rocks*, 485–494.
4. Karstunen M, Krenn H, Wheeler SJ, et al. (2005) Effect of anisotropy and destructuration on the behavior of Murro test embankment. *Int J Geomech* 5: 87–97. https://doi.org/10.1061/(ASCE)1532-3641(2005)5:2(87)
5. Rouainia M, Muir Wood D (2000) A kinematic hardening constitutive model for natural clays with loss of structure. *Géotechnique* 50: 153–164. https://doi.org/10.1680/geot.2000.50.2.153
6. Di Mariano A, Amoroso S, Arroyo M, et al. (2019) SDMT-based numerical analyses of deep excavation in soft soil. *J Geotech Geoenviron Eng* 145: 4018102. https://doi.org/10.1061/(ASCE)GT.1943-5606.0001993
7. González NA, Arroyo M, Gens A (2009) Identification of bonded clay parameters in SBPM tests: a numerical study. *Soils Found* 49: 329–340. https://doi.org/10.3208/sandf.49.329
8. Rouainia M, Panayides S, Arroyo M, et al. (2020) A pressuremeter-based evaluation of structure in London Clay using a kinematic hardening constitutive model. *Acta Geotech* 15: 2089–2101. https://doi.org/10.1007/s11440-020-00940-w
9. Monforte L, Gens A, Arroyo M, et al. (2021) Analysis of cone penetration in brittle liquefiable soils. *Comput Geotech* 134: 104123. https://doi.org/10.1016/j.compgeo.2021.104123
10. Fetrati M, Galavi V, Goodarzi M, et al. (2024) Simulation of cone penetrometer tests in sand using three advanced constitutive models: A comparative study. *Comput Geotech* 176: 106683. https://doi.org/10.1016/j.compgeo.2024.106683
11. Monforte L, Hauser L, Arroyo M (2025) Numerical studies of DMT insertion in fine grained soils. CIMNE Report to Marchetti S.P.A. Available from: https://www.marchetti-dmt.it.
12. Hauser L, Oberhollenzer S, Marte R, et al. (2025) Characterization of Microstructure of a Postglacial Deposit Based on In Situ Testing, Laboratory Testing, and Numerical Analysis. *J Geotech Geoenviron Eng* 151: 4025029. https://doi.org/10.1061/JGGEFK.GTENG-11985
13. Gundersen A, Hansen R, Lunne T, et al. (2019) Characterization and engineering properties of the NGTS Onsøy soft clay site.

14. Gundersen AS, Hansen RC, Bazin S, et al. (2019) Field and Laboratory Test Results from NGTS soft clay site—Onsøy. *Norges Geotekniske Institutt (NGI)*.
15. Gundersen AS, Lindgård A, Lunne T (2020) Impact of cone penetrometer type on measured CPTU parameters at 4 NGTS sites. Silt, soft clay, sand and quick clay. *Norges Geotekniske Institutt (NGI)*.
16. Doherty JP, Gourvenec S, Gaone FM, et al. (2018). A novel web based application for storing, managing and sharing geotechnical data, illustrated using the national soft soil field testing facility in Ballina, Australia. *Comput Geotech* 93: 3–8. https://doi.org/10.1016/j.compgeo.2017.05.007
17. Monaco P, Chiaradonna A, Marchetti D, et al. (2024) GEOLAB—Transnational Access project JELLYFISh—Field testing of Medusa DMT (Versione 1) [Data set]. Zenodo. https://doi.org/10.5281/zenodo.7695739
18. Oberhollenzer S, Lande E, Ritter S (2024) The influence of soil structure on CPTu and SDMT results. *7th International Conference on Geotechnical and Geophysical Site Characterization*. https://www.scipedia.com/public/Oberhollenzer*_et_al_2024a.
19. Monaco P, Chiaradonna A, Marchetti D, et al. (2024) Medusa SDMT testing at the Onsøy geo-test site, Norway. *E3S Web of Conferences*, 544: 02002. https://doi.org/10.1051/e3sconf/202454402002
20. Monaco P, Chiaradonna A, Marchetti D, et al. (2024) The JELLYFISh Project: Medusa SDMT testing at the NGTS Geo-Test sites, Norway. *7th International Conference on Geotechnical and Geophysical Site Characterization*, 18: 21. https://doi.org/10.23967/isc.2024.205
21. Lunne T, Berre T, Strandvik S (1998) Sample disturbance effects in deepwater soil investigations. *SUT Offshore Site Investigation and Foundation Behaviour New Frontiers: Proceedings of an International Conference*, 199–220.
22. Hight DW (2003) Sampling effects in soft clay: An update on Ladd and Lambe (1963). *Soil Behav Soft Ground Constr*, 86–121. https://doi.org/10.1061/40659(2003)4
23. Lunne T, Strandvik S, Kasin K, et al. (2018) Effect of cone penetrometer type on CPTU results at a soft clay test site in Norway, *Cone Penetration Testing 2018*, CRC Press.
24. Ching J, Phoon KK (2015) Constructing multivariate distributions for soil parameters, *Risk and Reliability in Geotechnical Engineering*, CRC Press. 3–76.
25. Monforte L, Arroyo M, Carbonell JM, et al. (2017) Numerical simulation of undrained insertion problems in geotechnical engineering with the Particle Finite Element Method (PFEM). *Comput Geotech.* 82: 144–156. https://doi.org/10.1016/j.compgeo.2016.08.013
26. Monforte L, Arroyo M, Carbonell JM, et al. (2018) Coupled effective stress analysis of insertion problems in geotechnics with the Particle Finite Element Method. *Comput Geotech* 101: 114–129. https://doi.org/10.1016/j.compgeo.2018.04.002
27. Dadvand P, Rossi R, Oñate E (2010) An object-oriented environment for developing finite element codes for multi-disciplinary applications. *Arch Comput Methods Eng* 17: 253–297. https://doi.org/10.1007/s11831-010-9045-2
28. Oñate E, Idehsohn SR, del Pin F, et al. (2004) The particle finite element method—an overview. *Int J Comp Meth* 1: 267–307. https://doi.org/10.1142/S0219876204000204
29. Monforte L, Carbonell JM, Arroyo M, et al. (2017) Performance of mixed formulations for the particle finite element method in soil mechanics problems. *Comp Part Mech* 4: 269–284. https://doi.org/10.1007/s40571-016-0145-0

30. Oliver J, Huespe AE, Cante JC (2008) An implicit/explicit integration scheme to increase computability of non-linear materials and contact/friction problems. *Comput Methods Appl Mech Eng* 197: 1865–1889. https://doi.org/10.1016/j.cma.2007.11.027
31. Monforte L, Ciantia MO, Carbonell JM, et al. (2019) A stable mesh-independent approach for numerical modelling of structured soils at large strains. *Comput Geotech* 116: 103215. https://doi.org/10.1016/j.compgeo.2019.103215
32. Carbonell JM, Oñate E, Suárez B (2010) Modeling of ground excavation with the particle finite-element method. *J Eng Mech* 136: 455–463. https://doi.org/10.1061/(ASCE)EM.1943-7889.0000086
33. Carbonell JM, Monforte L, Ciantia MO, et al. (2022) Geotechnical particle finite element method for modeling of soil-structure interaction under large deformation conditions. *J Rock Mech Geotech Eng* 14: 967–983. https://doi.org/10.1016/j.jrmge.2021.12.006
34. Yu HS (1998) CASM: a unified state parameter model for clay and sand. *Int J Numer Anal Methods Geomech* 22: 621–653. https://doi.org/10.1002/(SICI)1096-9853(199808)22:8<621::AID-NAG937>3.0.CO;2-8
35. Gonzalez NA (2011) Development of a family of constitutive models for geotechnical applications. PhD thesis. Universitat Politècnica de Catalunya.
36. Arroyo M, Ciantia M, Castellanza R, et al. (2012) Simulation of cement-improved clay structures with a bonded elasto-plastic model: A practical approach. *Comput Geotech* 45: 140–150. https://doi.org/10.1016/j.compgeo.2012.05.008
37. Abbo AJ, Lyamin AV, Sloan SW, et al. (2011) A C2 continuous approximation to the Mohr-Coulomb yield surface. *Int J Solids Struct* 48: 3001–3010. https://doi.org/10.1016/j.ijsolstr.2011.06.021
38. Mánica MA, Arroyo M, Gens A, et al. (2022) Application of a critical state model to the Merriespruit tailings dam failure. *Proc Inst Civ Eng Geotech Eng* 175: 151–165. https://doi.org/10.1680/jgeen.21.00001
39. Marchetti S, Monaco P, Totani G, et al. (2001) The Flat Dilatometer Test (DMT) in Soil Investigations—A Report by the ISSMGE Committee TC16. *Proc. Int. Conf. Insitu Measurement of Soil Properties and Case Histories*, Bali, 95–131. Official version approved by ISSMGE TC16 reprinted in Proc. 2nd Int. Conf. Flat Dilatometer, Washington, 2006, 7–48. Available from: https://www.marchetti-dmt.it/.
40. Butlanska J, Arroyo M, Amoroso S, et al. (2018) Marchetti flat dilatometer tests in a virtual calibration chamber. *Geotech Test J* 41: 930–945. https://doi.org/10.1520/GTJ20170370
41. Kouretzis GP, Ansari Y, Pineda J, et al. (2015) Numerical evaluation of clay disturbance during blade penetration in the flat dilatometer test. *Geotech Lett* 5: 91–95. https://doi.org/10.1680/jgele.15.00026
42. Yu HS, Carter JP, Booker JR (1993) Analysis of the dilatometer test in undrained clay. *Predictive soil mechanics: Proceedings of the Wroth Memorial Symposium held at St Catherine's College*, Oxford, Thomas Telford Publishing. 783–795.
43. Colcott R, Lehane BM (2012) The design, development and application of a new DMT. *Geotechnical and Geophysical Site Characterization: Proceedings of the 4th International Conference on Site Characterization ISC-4*, Taylor & Francis Books Ltd, 565–570.

44. Robertson PK (2009) Interpretation of cone penetration tests—a unified approach. *Can Geotech J* 46: 1337–1355. https://doi.org/10.1139/T09-065
45. Monforte L, Arroyo M, Gens A (2022) Undrained strength from CPTu in brittle soils: a numerical perspective, *Cone Penetration Testing 2022*, CRC Press.
46. Plewes HD, Davies MP, Jefferies MG (1992) CPT based screening procedure for evaluating liquefaction susceptibility. *Proceedings of the 45th Canadian Geotechnical Conference*, Toronto, Canada, 4: 1–9.
47. Jefferies M, Been K (2015) *Soil liquefaction: a critical state approach*, second edition, London, United Kingdom. CRC Press.
48. Robertson PK (1990) Soil classification using the cone penetration test *Can Geotech J* 27: 151–158.
49. Schneider J, Randolph MF, Mayne PW, et al. (2008) Analysis of factors influencing soil classification using normalized piezocone tip resistance and pore pressure parameters. *J Geotech Geoenviron Eng* 134: 1569–1586. https://doi.org/10.1061/(ASCE)1090-0241(2008)134:11(1569)
50. Lunne T, Long M, Forsberg CF (2003) Characterisation and engineering properties of Onsøy clay. *Charact Eng Prop Nat Soils* 1: 395–428.
51. Lacasse S, Lunne T (1982) Penetration tests in two Norwegian clays. Norwegian Geotechnical Institute Publication, 138.
52. Hauser L, Durán Caballero DE, Monforte Vila L, et al. (2024) Numerical study of viscous effects during CPTu. *ISC'7: 7th International Conference on Geotechnical and Geophysical Site Characterization*, International Centre for Numerical Methods in Engineering (CIMNE), 1741–1745. https://doi.org/10.23967/isc.2024.261
53. Grimstad G, Degago SA, Nordal S, et al. (2010) Modeling creep and rate effects in structured anisotropic soft clays. *Acta Geotech* 5: 69–81. https://doi.org/10.1007/s11440-010-0119-y

AIMS Press